2015

Evaluation of Key Geomechanical Aspects of Shallow and Deep Geothermal Energy

Robert Alexander Caulk
University of Vermont

Evaluation of Key Geomechanical Aspects of Shallow and Deep Geothermal Energy

A Thesis Presented

by

Robert Caulk

to

The Faculty of the Graduate College

of

The University of Vermont

In Partial Fullfillment of the Requirements
for the Degree of Master of Science
Specializing in Civil and Environmental Engineering

October, 2015

Defense Date: May 18, 2015

Thesis Examination Committee:
Ehsan Ghazanfari, PhD., Advisor
Julia Perdrial, Ph.D., Chairperson
Mandar Dewoolkar, Ph.D.
Donna Rizzo, Ph.D.
Cynthia J. Forehand, Ph.D., Dean of the Graduate College

Abstract

Geothermal energy has become a focal point of the renewable energy revolution. Both shallow and deep types of geothermal energy have the potential to offset carbon emissions, reduce energy costs, and stimulate the economy. Before widespread geothermal exploration and exploitation can occur, both shallow and deep technologies require improvement by theoretical and experimental investigations. This thesis investigated one aspect of both shallow and deep geothermal energy technologies. First, a group of shallow geothermal energy piles was modeled numerically. The model was constructed, calibrated, and validated using available data collected from full-scale in-situ experimental energy piles. Following calibration, the model was parameterized to demonstrate the impact of construction specifications on energy pile performance and cross-sectional thermal stress distribution. The model confirmed the role of evenly spaced heat exchangers in optimal pile performance. Second, experimental methods were used to demonstrate the evolution of a fractured granite permeability as a function of mineral dissolution. Steady-state flow-through experiments were performed on artificially fractured granite cores constrained by 5 MPa pore pressure, 30 MPa confining pressure, and a 120^oC temperature. Upstream pore pressures, effluent mineral concentrations, and X-Ray tomography confirmed the hypothesis that fracture asperities dissolve during the flow through experiment, resulting in fracture closure.

Acknowledgements

I would like to thank several people and entities for contributing to the thesis. First, I would like to thank Dr. John McCartney for providing access to field data and continuously supporting the project with analysis and results. I want to thank Dr. Julia Perdrial and Dr. Nico Perdrial for providing assistance with experimental setup and analysis. I also want thank my other committee members, Dr. Mandar Dewoolkar and Dr. Donna Rizzo for key advice throughout my degree. I would like to thank Garrett Gissler for his assistance with thin-section analysis and Marco vanGemeren for his coring and lapping expertise. The research presented in this thesis would not have been possible without the Teaching Assistant funding support from Civil and Environmental Engineering at the University of Vermont. I would like to acknowledge the Vermont Advanced Computing Core supported by NASA (NNX 06AC88G), for providing High Performance Computing Resources that contributed to the research results reported within this thesis. I would also like to acknowledge the Vermont Space Grant Consortium for additional funding. Finally, I would like to thank my advisor, Dr. Ehsan Ghazanfari, for his guidance and encouragement.

Dedication

This thesis is dedicated to my grandfather, Dominic Caruso, for his hard work and intelligent foresight, both of which enabled my extended education and fostered my curiosity.

Table of Contents

List of Figures

Chapter 1

Introduction

The finite availability and environmental concerns associated with fossil fuels have ushered in an array of renewable energy alternatives in recent decades. Geothermal energy represents one of the more dependable and versatile renewable alternatives due to the ubiquitous availability, low operating costs, and low carbon emissions. Not only can geothermal energy lessen residential heating/cooling bills (shallow geothermal energy), but it can also generate baseload power for the electrical grid (deep geothermal energy). Both products, climate control and electricity, are unarguably beneficial, however the sustainability of these products depends on the methods and technologies used to extract geothermal energy. At the time of this writing, the uncertainty associated with deep geothermal energy extraction sustainability remains too high for a commercialized industry to emerge. On the other hand, shallow geothermal energy extraction is well proven and generally successful. However, shallow geothermal energy applications continue to grow in size and demand and require additional research to increase performance and efficiency.

This introduction provides the reader with a basic understanding of shallow and deep geothermal energies. In the context of this thesis, the introduction introduces both shallow and deep geothermal energies and then identifies and extrapolates upon specific methods

and terms necessary to support the core of the thesis presented.

1.1 Shallow Geothermal Energy

Thermal energy stored between 0 - 50 m below the Earth's surface is considered "shallow geothermal energy". Although seasonal temperature fluctuations influence the amount of thermal energy stored subterraneously between 0 and 5 m (15 ft), a near constant subsurface temperature between 10-15 ^oC can be observed below this depth. Given the overwhelming amount of thermal energy stored at these depths, the subsurface can be considered a source or a sink for all heat pump intents and purposes.

1.1.1 The Role of the Heat Pump

Heat pump technology is well established, and continues to refrigerate food (refrigerator) and even cool/heat homes (air source heat pump). The general concept of the heat pump involves three closed fluid circulation loops (Fig. 1.1) . The first heat exchange loop extracts heat from a low density heat source. The fluid carries the heat to a second loop where fluid absorbs the low density heat and electrical power compresses the heat. A third loop, called the distribution loop, then absorbs the high density heat from the second loop and delivers it to an environment that is fully separated from the first loop. In the case of a Ground Source Heat Pump (GSHP), the first loop is embedded in soil and the distribution loop is installed in a building (Fig. 1.1).

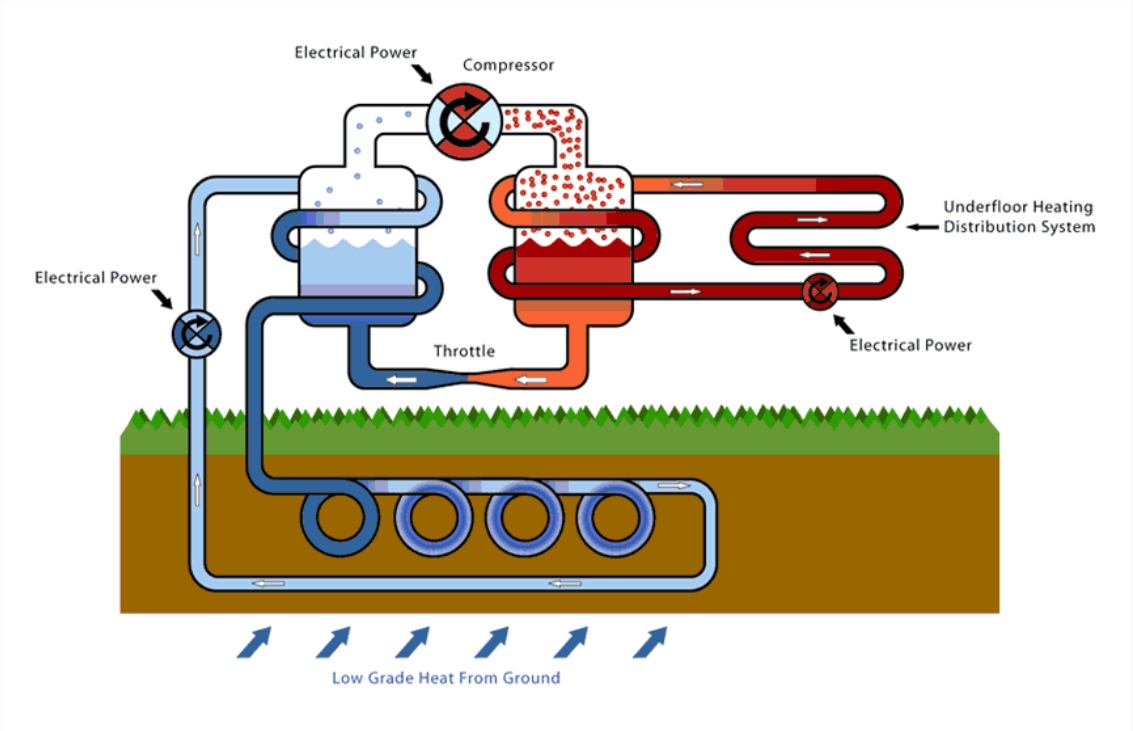

Figure 1.1: Ground Source Heat Pump Schematic
Source: Mott MacDonald Engineering

1.1.2 Advantages and Disadvantages of the GSHP

The benefits associated with the GSHP system generally outweigh any disadvantages. An incredible 300% efficiency dwarfs that of traditional oil/gas boilers and results in 30-50% reduced operational and maintenance costs (Mustafa Omer, 2008). In contrast to conventional indoor heating and cooling systems, the GSHP requires electrical input, linking it with a strong resistance to oil price fluctuations. Another advantage of the GSHP is the cleanliness of the heat distribution. Conventional systems rely on air ducts for convective forced hot air, while the GSHP system delivers "clean" heat via radiant floor or baseboard heating. Another commonly overlooked benefit is the versatility of the GSHP. A properly installed GSHP has the ability to not only heat, but also cool a home or building. The final invaluable benefit associated with a GSHP system is the lack of carbon dioxide emissions.

If the GSHP is coupled with solar energy (common configuration) it generates zero carbon emissions. GSHP systems are unarguably a genuine renewable alternative to traditional climate control systems, but they are associated with some disadvantages.

Many disadvantages associated with GSHP systems can be mitigated or justified rather easily. The installation cost of a GSHP system remains the main barrier between many homeowners and green climate control. This cost can reach $20,000 for a closed-loop ground source system. Although this initial cost is steep, the annual operational costs can be half as expensive as operational costs for a conventional system (Mustafa Omer, 2008). The majority of the initial cost lies in the borehole drilling and installation of the heat exchange tubes. Many commercial buildings mitigate this problem by embedding the heat exchanger tubes in the load bearing concrete foundation piles (Fig. 2.1). Accordingly, drilling costs are avoided and installation costs are sharply decreased. Furthermore, concrete foundation piles are not the only foundational structures available to be outfit with heat exchangers. Concrete retaining walls, slabs, and abutments are all energy geo-structures suited to be outfit with heat exchangers at a low cost for a high benefit (Laloui and Di Donna, 2013). These "geo-structures" combine the existing need to direct building loads into the ground with energy supply.

1.1.3 The Role of Energy Piles

Concrete energy piles are a natural fit for the efficient use of geothermal energy. Heat exchangers embedded within the energy piles facilitate heat transfer between the working fluid and the subsurface. Since concrete foundation piles can range in length (depth) from 10-50 m (Brandl, 2006), they provide access to the constant subsurface temperatures necessary for an efficient GSHP system. Another inherent benefit is the high thermal conductivity of

concrete. This results in quick transfer of heat between the embedded heat exchangers and the surrounding soil. Finally, the concrete protects the heat exchangers from weathering deterioration and ground shifting.

Heat exchanger configurations vary for energy piles. The most common types are referred to as U-shape and W-shape. U-shape heat exchangers form a U within the energy pile, and accordingly the W-shape describes a W-shaped heat exchanger (Fig. 1.2).

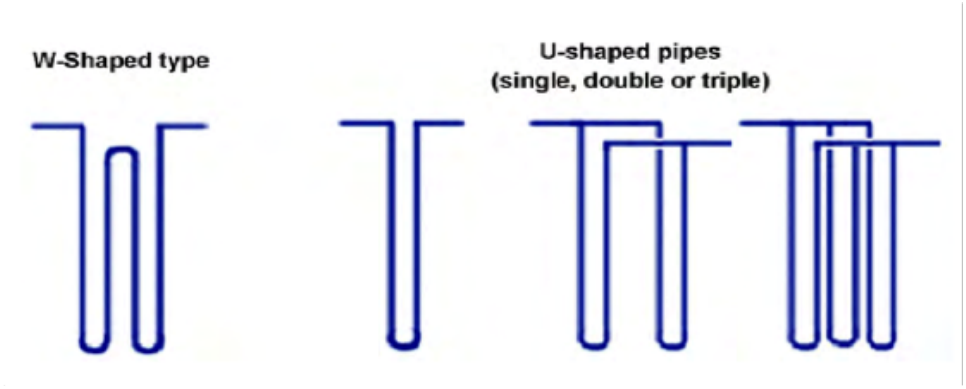

Figure 1.2: Comparison between W-shape and U-shape heat exchangers

1.2 Deep Geothermal Energy

1.2.1 Overview of Deep Geothermal Energy

Thermal energy stored between 2-10 km below the Earth's surface is considered "Deep Geothermal Energy". Deep Geothermal Energies are generally categorized by their hydrogeological characteristics. Liquid dominated geothermal reservoirs are characterized by hot water (100-200^oC) stored in the Earth's crust slowly escaping via surface anomalies (geysers, hot springs, etc.). Most geothermal operations extract hot water from liquid dominated reservoirs by pumping water out of the reservoir. Following extraction, the hot water

is used to turn a turbine and generate electricity. The Nesjavallir Geothermal Power station in Iceland is a successful demonstration of geothermal energy extraction from a liquid dominated reservoir. Contrary to liquid dominated reservoirs, vapor dominated reservoirs store hot water vapor. These reservoirs do not require pumping for hot fluids, which results in increased efficiency. The Geysers of Northern California is a successful demonstration of geothermal energy extraction from a vapor dominated reservoir. The third type of deep geothermal energy is referred to as an Enhanced Geothermal System (EGS). These systems rely on hot (150-250 ^oC) dry rock at depths of 3-5 km. Currently there are few EGS operations, however the operations that are ongoing are exhibiting great progress (Habanero - Cooper Basin, AU; Newberry Volcano - Bend, Oregon, USA; Soultz FR).

1.2.2 Enhanced Geothermal Systems

An EGS truly is an engineered system (Fig. 1.3). The system accesses thermal energy stored deep within the Earth's crust (3-5 km). This is accomplished by drilling an injection well and a production well $\approx$3 km deep and 10-800 m apart (MIT Report, 2006). The space between the wells requires pressurized stimulation to open up existing fractures in the hot rock matrix. Once both wells are connected by fractures, water that is colder than the surrounding rock matrix (80-100^oC) is pumped into the injection well and hot water (150-250 ^oC) is extracted from the production well. The hot water is then used to drive a turbine and generate power. This process can be considered an engineered liquid dominated reservoir. As one might expect, the engineering challenges are associated with great uncertainty. However, according to MIT Report (2006), EGS has the potential to generate 100,000 MWe of baseload power to the United States electric grid alone.

Several hurdles stand between a potential EGS and a fully operational power plant. The

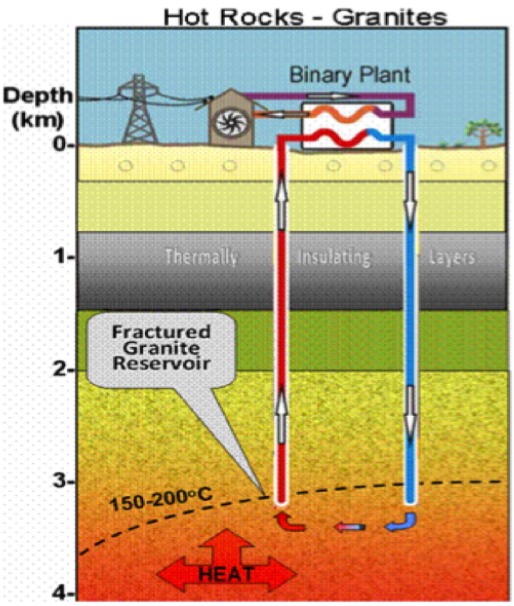

Figure 1.3: Enhanced Geothermal System diagram
Source: Raya Group

first hurdle is the estimation of a subsurface temperature gradient in the area of interest. Temperature gradients vary drastically throughout the Earth's crust making estimation difficult in regions where oil/gas drilling records are unavailable. In general, it is desirable to encounter temperatures of 200^oC between 3-4 km depth. These temperatures are achievable in regions of moderate to high crustal heat flow. For example, the western region of the United States exhibits high crustal heat flow which may be suitable for EGS.

After the wells are drilled (which is an engineering feat in itself), the next hurdle is reservoir characterization. First, existing fractures are identified using boring-logs, borehole imaging, geophysical logs, cores, and existing oil/gas drilling records. Following the identification of existing fractures, the in-situ stresses are estimated. Minimum and maximum horizontal stresses are estimated using various theoretical methods (Evans et al., 1999; MIT Report, 2006; Ghassemi, 2012). These stresses play an important role in understanding potential seismicity, drilling feasibility, reservoir stimulation, and permeability evolution.

Additionally, these stresses aid in stimulation design (i.e. the prediction of required pore pressure magnitude and the resulting propagation extent and direction of fractures.)

Stimulation of the reservoir may be the most important step to developing a successful EGS. Water is pumped into the wells at high pressures, which lowers the effective stress of the rock and opens existing fractures perpendicular to the minimum horizontal stress in the reservoir. This process is, however, more complicated than previously thought. In addition to in-situ stress states, thermoporoelastic effects play an important role in fracture initiation and propagation (Tarasovs and Ghassemi, 2012). Furthermore, fractures may occur due to tensile fracturing and shear-slip fracturing in addition to conventional propagation fracturing (Ghassemi and Zhang, 2004). In an effort to manage these variables, micro-seismic waves released from the fractured rock are observed and triangulated during stimulation. These triangulated measurements are used to map the size and extent of stimulated fractures between wells. In this way, the observations can be used to modify stimulation techniques by identifying well depths that may encourage fracture propagation in the desired direction (toward the coupled production/injection well).

Reservoir mapping plays an important role in stimulation, operation, maintenance, and safety of an EGS. Fracture-cloud mapping technologies have been adopted from the shale gas industry. A combination of tracers, microseismic monitoring, and advanced tomography modeling techniques are all used to map the fracture-cloud and detect fracture connectivity/permeability (Ghassemi, 2012). These techniques provide crucial feedback to EGS operators. First, operators can use feedback to monitor induced seismicity within the reservoir. Induced seismicity occurs when stored energy is released from prestressed rock at depth. Records show that induced seismicity can cause upwards of 2.5 ML on the Richter scale (Basal, Switzerland - minor damage caused to buildings). Although seismicity of this mag-

nitude is rare and easily avoided (Basal sits on a locked fault, and seismicity was expected), it is important for operators to avoid possible inconveniences to surrounding towns. Second, operators can use feedback to properly schedule zone isolated re-stimulations throughout the lifecycle of the EGS. These re-stimulations maintain production flow rates and temperatures. Although the mapping tools mentioned here are great for understanding the response of an EGS, they do not directly address the reduced permeability associated with reduced productivity.

Once the reservoir is fully mapped and the coupled injection/production wells are sufficiently connected, an energy conversion system must be selected and installed. Generally, the production fluid flow rate and temperature dictate the selection of the conversion system. For lower flow rates and temperatures (19.5 kg/s and 150-200^oC), a basic binary energy conversion system is most appropriate. Higher flow rates and temperatures (425 kg/s and 250^oC) require a flash system (Li and Lior, 2014). These systems are distinguished by the indirect (binary) and direct (flash) use of the geofluid extracted from the reservoir, however, both systems employ a turbine for the power generation.

Several problems manifest following normal operation of an EGS power plant. The first issue encountered is well-bore scaling. Scaling occurs due to pressure and temperature changes associated with producing geo-fluids from 3-5 km depth. These pressure and temperature changes result in precipitation and deposition of calcium carbonate and silica scale. The scaling clogs the wells and corrodes surface equipment resulting in lowered flow rates and maintenance down times. Although calcium carbonate is easily managed using polymaleic acids, silica scale is much more difficult to deal with. *Another problem associated with normal EGS operation is the reduction of reservoir permeability.* As working fluids dissolve the rock and redeposit mineral mass from the matrix to the well bore and surface

equipment, the fractures close due to what is hypothesized as fracture surface asperity dissolution and fracture face skin ('weathered' fracture surface resulting in lower conduction of water to the rock matrix). Another potential problem that arises with normal operation is the creation of highly conductive conduits within larger fractures. These conduits attract more water and tend to grow with time. The result is referred to as a "short-circuit" and results in increased production flow rate, but sharply decreased production temperatures as a result of reduced fluid residence time (and heat transferred).

Enhanced Geothermal Systems are an incredible feat of systems engineering. Starting with geological exploration, moving to drilling through several kilometers of dense rock, continuing to the engineered fractured system at depth, and finishing with the installation of an energy conversion system. The process is riddled with uncertainty and potential setbacks. One of the main sources of uncertainty is associated with permeability evolution. Therefore, the research presented in Chapter 3 attempts to experimentally investigate this uncertainty.

1.3 Research Objective

The objective of this research is to improve the state of knowledge for shallow and deep geothermal energy technologies. Shallow and deep geothermal energy technologies suffer from the same shortcoming: long-term sustainability. Research is ongoing to improve modern technologies, but remains insufficient. Further investigation of rock-water interactions under coupled physiochemical processes in EGS should be conducted to better understand permeability decreases over time. Additional field and numerical research needs to be completed on energy piles to better define the relationships between construction specifications and performance. Although many ongoing and past studies have attempted to address these shortcomings, they have failed to fully capture the complex relationships described

above. Once these relationships are fully defined, long-term deep and shallow geothermal sustainability will be regarded with increased certainty.

Shallow geothermal energy pile applications are increasing in size and demand, while the relationship between simple design specifications and performance remains undeveloped. The research presented within this thesis employs numerical modeling techniques to gain insight into the role of construction specifications on energy pile performance and thermal stress distribution. Concrete cover, shank distance, and pile spacing can be optimized for maximum heat extracted/rejected. Chapter 2 details the methods and results used to support this hypothesis.

Like geothermal energy pile applications, existing EGS have not operated long enough to observe long-term rock-water behaviors. However, even short-term observations indicate a strong reduction in production temperatures and flow rates (MIT, 2006). The research presented within this thesis uses a novel experimental procedure to demonstrate the dissolution of fracture surface asperities and the associated fracture aperture decrease. As these asperities dissolve, the fractures close, and flow rate is reduced. Chapter 3 details the methods and results used to evaluate this hypothesis.

Chapter 2

Journal Paper - Parameterization of a calibrated geothermal energy pile model

Authors: Robert Caulk[1], Ehsan Ghazanfari, PhD[1], John McCartney, PhD[2]

Submitted to Geomechanics for Energy and the Environment

[1] University of Vermont, Department of Civil and Environmental Engineering

[2] University of California, San Diego, Department of Structural Engineering

2.1 abstract

This paper describes the calibration and parameterization of a numerical model for conductive heat transfer from a group of geothermal energy piles into the soil surrounding the piles. Calibration was performed using Thermal Response Test (TRT) data collected from a group of full-scale in-situ geothermal energy piles in Colorado Springs, CO. The calibration of the three dimensional model incorporated field data to represent boundary conditions including inlet temperature, atmospheric temperature, and subsurface temperatures at different locations within the pile group. Following calibration, the model was parameterized to understand the role of heat exchanger configuration with a given energy pile as well as the role of pile spacing in an energy pile group. Parametric combinations were compared using heat transfer per unit length of the energy pile (W/m). The results of the parametric study indicate that heat transfer from energy piles increases by up to 8% for an even heat

exchanger layout compared to an uneven layout. These results also provide useful insight into the cross-sectional temperature distribution of an energy pile. Energy pile temperature was observed to vary by up to 20% across the core of the pile during heating for various heat exchanger layouts. This uneven temperature distribution may have implications on the estimation of in-situ energy pile thermal axial stresses; strain gage measurements at the reinforcing cage may underestimate thermal axial stress during heating.

keywords: Geothermal Energy, Energy Pile, Numerical Modeling, COMSOL , Calibration, Thermo-active foundation

2.2 Introduction

Indoor climate control accounts for almost 50% of America's residential energy consumption (EIA, 2011). As energy prices rise with increased demand and short supply, global communities will need clean renewable alternatives to heat/cool residential and commercial buildings. Although ground source heat pumps are a well-established energy efficiency technology, their coupling to building foundations provides a new way to transfer heat to or from the ground for lower installation costs. Heat is transferred by circulating heated or cooled fluid through closed-loop heat exchangers embedded in the foundations. In this way, geothermal energy piles serve two purposes, first to transfer building loads into the subsurface, but also to extract thermal energy from surrounding soils.

Concrete energy piles are a natural fit for geothermal energy. Since concrete foundation piles are generally longer than 6 m (Brandl, 2006), they provide access to the constant subsurface temperatures necessary for an efficient ground source heat pump (GSHP) system. Another benefit is the reduced heat exchanger installation cost compared to traditional vertical borehole heat exchangers. Since the installation of foundation piles requires drilling equipment, heat exchangers do not require additional installation (drilling) cost. Also, geothermal energy piles are easily coupled with solar panels to provide grid-independent climate control. Finally, the concrete protects the heat exchangers from damage and re-

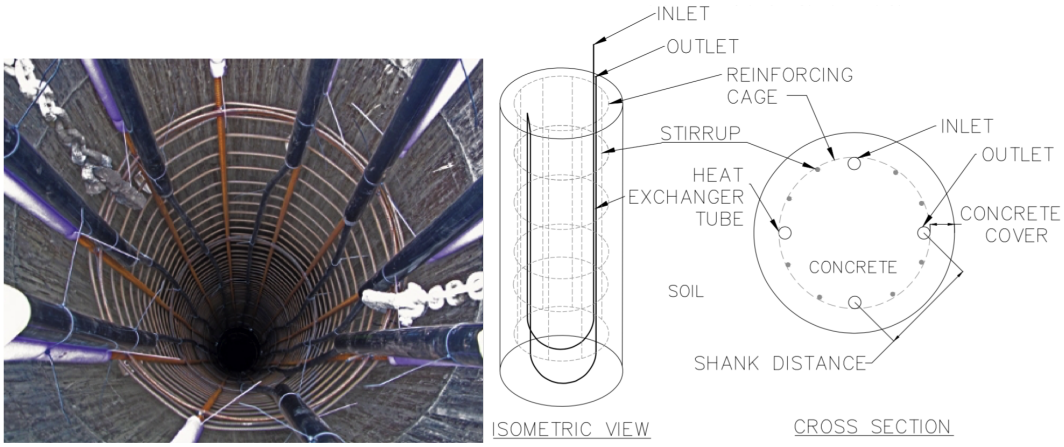

Figure 2.1: Image and sketch showing heat exchanger pipes embedded in concrete energy piles with geometry details relevant to thermal performance

strains potential ground water pollution (Brandl, 2006).

Geothermal energy piles need to remain operational for the lifespan of the building they are supporting. Therefore, the initial design must accommodate for maximizing thermal performance and characterizing the thermal stresses associated with the thermal soil-structure interaction (Bourne-Webb et al., 2014). The cross-sectional temperature distributions within energy piles not only reflect the transient heat transfer characteristics of the geothermal energy pile, but may also have an important impact on the in-situ thermal axial stress within the energy pile (Murphy and McCartney, 2015). The objective of this study is to employ numerical modeling techniques to better understand the role of construction specifications on the thermal and thermo-mechanical performance of energy piles, as well as on their cross-sectional temperature distributions. Concrete cover, shank distance, and pile spacing contribute to both the amount of heat transferred from an energy pile into surrounding soils, as well as the cross-sectional temperature/thermal axial stress distribution. In the context of this study, concrete cover is defined as the minimum distance between the heat exchanger and the outer edge of the concrete pile and shank distance is defined as the width of the downward U loop heat exchangers as shown in Fig. 2.1.

In an attempt to provide insight into geothermal energy pile behavior, the present study details the calibration, validation, and parameterization of a model followed by a discussion of results and concluding remarks. COMSOL Multi-physics software and high-performance computing (HPC) enabled the construction of the full-scale three-dimensional finite element model. The model was calibrated with respect to an experimental field investigation conducted at the United States Air Force Academy (USAFA) in Colorado Springs, CO (Murphy et al., 2015). Accordingly, all geometries within the model reflect full-scale, in-situ geometries of the experimental energy piles and surrounding soil strata. The full-scale model coupled conductive heat transfer and non-isothermal pipe flow physics to estimate temperatures at any time/location within the model. Calibration was performed by comparing these model temperatures to field temperatures. Following calibration, the model was parameterized to understand the roles of concrete cover, shank distance, and pile spacing on heat transfer from energy piles into surrounding soils. The heat transfer performance of the energy pile group was evaluated, and relationships between construction specifications and performance were quantified. These relationships verified the model. The model was also used to investigate the evolution of the cross-sectional temperature distribution within the energy pile and examine the implications of strain gage location on in-situ thermal axial stress estimation. Most importantly, this study exhibits the variation of energy pile performance with respect to construction specifications and the evolution of cross-sectional temperature distribution, which is key to the improvement of geothermal energy piles. This study also demonstrates the strength and flexibility of the finite element based model and the capabilities of COMSOL coupled with HPC.

2.3 Background

Evaluating heat transfer between geothermal energy piles and surrounding soils remains a key area of research numerically [Gao et al. (2008);Wood et al. (2009);Suryatriyastuti et al. (2012);Park et al. (2013);Abdelaziz et al. (2014); Gashti et al. (2014);Wang et al. (2014);Jalaluddin and Miyara (2014);Ozudogru et al. (2014)] and in the field [Laloui et al. (2006); Hamada et al. (2007); Bourne-Webb et al. (2009);Loveridge and Powrie (2012);Olgun et al. (2012);Murphy et al. (2015) ;McCartney et al. (2015); Abdelaziz et al. (2015)]. Field experiments performed by Hamada et al. (2007) and Gao et al. (2008) were designed to evaluate the most efficient heat exchanger layout within energy piles. With respect to thermo-mechanical processes, Bourne-Webb et al. (2009) used an experimental pile embedded in London Clay to investigate energy pile behavior during cyclic heating. More recently, Murphy et al. (2015) and Murphy and McCartney (2015) detailed the thermo-mechanical response of in-situ energy piles in different soil profiles. The interest in energy pile behavior has motivated the development of energy pile design guidelines.

A state of practice paper by Bourne-Webb et al. (2014) emphasized the current need for advanced finite element models in addition to field studies to improve existing design guidelines for geothermal energy piles. Existing energy pile design guidelines are contained within GSHPA (2012), however these guidelines focus on sizing and installation “best practices". In an attempt to move towards energy pile design guidelines that incorporate the thermally influenced pile-soil interface, Mimouni and Laloui (2014) conducted a combined numerical-experimental study. The study demonstrated the dynamic loading, expansion/contraction, and associated friction mobilization inherent to energy piles. Another key numerical study relating to the design of energy piles was performed by Cecinato and Loveridge (2015). The study investigated the influences of design parameters on energy pile efficiency using an

analytically-validated numerical model and parametric statistical methods. These methods enabled the quantified contribution of several key design parameters including pile length, number of heat exchangers, and concrete cover. Cecinato and Loveridge (2015) expressed the importance of increasing the number of heat exchanger tubes to maximize efficiency. Different from the study of Cecinato and Loveridge (2015), this study incorporates full soil and foundation material calibration with the investigation of the role of design parameters on the cross-sectional temperature distribution for energy piles with W-shaped heat exchanger layouts.

Several other studies have focused on numerically and analytically modeling heat exchangers embedded within grout and concrete foundation piles. Abdelaziz et al. (2014) used a multilayer finite line source model of an energy pile to address ground stratification and thermally induced moisture migration. The study stressed the importance of incorporating multiple soil layers into any energy pile model. Ozudogru et al. (2014) validated a three dimensional COMSOL model with a finite line source analytical model and concluded that this methodology can successfully simulate the operation of heat exchangers embedded within soil. Gashti et al. (2014) investigated thermal regimes within steel energy piles using a three dimensional numerical analysis in COMSOL. The study yielded insight into the performance of U-tube configurations (1 vs 2 U-tubes) and a range of flow rates, however the main conclusion was that the thermal behavior within energy piles is inherently complex and requires three dimensional analysis (i.e. the assumption of a constant temperature along the length of an energy pile is insufficient to fully understand energy pile behavior). Another numerical study conducted by Kaltreider et al. (2015) investigated the design parameters of an energy foundation using a three dimensional numerical approach coupled with an experimental validation. The study focused on a U-shaped heat exchanger and concluded that flow rate, soil properties, and foundation depth contribute significantly

to the heat flux from the floor slab to the building. Collectively, the aforementioned experiments and numerical/analytical investigations demonstrate the existing interest in heat exchanger layouts and the demand for a better understanding of the relationships between construction specifications and energy pile behavior/performance.

Many of the past and current energy pile field studies investigated the development of thermal axial strain and associated stresses within field piles using strain gages embedded within the piles (e.g. Murphy et al. (2015)). Murphy and McCartney (2015) observed that there may be issues in calculating the thermal axial stress in energy piles from strain gage measurements due to nonhomogenous cross-sectional temperatures within the energy piles. Specifically the strain within an energy pile is likely governed by the average cross-sectional temperature; however, the gage temperature may be up to 4^oC different than the average cross-sectional temperature (Loveridge and Powrie, 2013; Murphy and McCartney, 2015). Because the equation of the thermal axial stress requires knowledge of the change in average temperature of the pile (Murphy et al., 2015), this observation implies that using the temperature measured at a point to characterize the thermal axial stress may lead to errors in the stress calculation. This source of error was identified by Murphy and McCartney (2015), where the thermal axial strains during foundation heating were slightly greater than the free expansion thermal axial strains calculated using the temperature at a point. This means that the calculated thermal axial stress would be in tension, which does not make sense physically. Accordingly, a better understanding of temperature distribution may improve estimates of the changes in thermal axial stress in energy piles.

2.4 Governing equations

The use of the commercial COMSOL Multi-physics finite element software package enabled the three dimensional modeling of coupled interactions between heat exchangers embedded within concrete energy piles and stratified soils. Non-isothermal pipe flow and basic conductive heat transfer physics interacted within these three distinct domains (heat exchangers, concrete energy pile, soil). Several key parameters were accounted for to approximate the differential equations presented below (Ghasemi-Fare and Basu, 2013). Thermal conductivity, k, specific heat capacity, C_p, and density, ρ, of the soils, concrete piles, and embedded heat exchangers contributed to the rate and amount of heat transferred within the system. Heat transfer within the concrete energy pile and the surrounding soils was computed using the aforementioned material properties with the conservation of energy equation, assuming no internal heat generation:

$$\rho C_p \frac{\partial T}{\partial t} = \boldsymbol{\nabla} \cdot (k \boldsymbol{\nabla} T), \tag{2.1}$$

where ρ is density $[kg/m^3]$ and C_p is heat capacity at constant pressure $[J/(kg * K)]$. The right-hand side of the equation is the net rate of heat conduction into the material; k is the thermal conductivity $[W/(mK)]$ and T is the temperature of the material $[K]$.

Equivalent $(\rho C_p)_e$ and k_e values were used with Eq. 2.1 to compute heat transfer through porous media (Darcy porous medium):

$$(\rho C_p)_e = \theta_p \rho_p C_p + (1 - \theta_p) \rho_{soil} C_p, \tag{2.2}$$

$$k_e = \theta_p \rho_p + (1 - \theta_p) k_{soil}, \tag{2.3}$$

where $(\rho C_p)_e$ and k_e are the overall heat capacity and thermal conductivity per unit volume. The density and thermal conductivity of the pore fluid (in this case air) represented by ρ_p and k_p. Thus, $(1 - \theta_p)$ is the ratio of the area occupied by the solids to the total cross-sectional area of the soil.

In order to model the multi-physics problem presented by the energy piles, heat exchanger fluid flow must be incorporated (Gashti et al., 2014). The study presented here used one-dimensional pipe elements to represent the heat exchangers. This simplified pipe flow approximation was accomplished using the conservation of momentum and continuity equations (Barnard et al., 1966):

$$\rho \frac{\partial \boldsymbol{u}}{\partial t} = -\boldsymbol{\nabla_t} p \cdot \boldsymbol{e_t} - \frac{1}{2} f_d \frac{\rho}{d_h} |u| u, \tag{2.4}$$

$$\frac{\partial A\rho}{\partial t} + \boldsymbol{\nabla_t} \cdot (A\rho u \boldsymbol{e_t}) = 0, \tag{2.5}$$

where p is the pressure in the heat exchanger $[N/m^2]$, $\boldsymbol{e_t}$ is the tangential unit vector along the edge of the pipe, f_d is the darcy friction factor, ρ is the density of the fluid $[kg/m^3]$, d_h is the hydraulic diameter of the pipe $[m]$, and u is the velocity of the pipe flow $[m/s]$, and A is the cross-sectional area of the pipe $[m^2]$.

Heat transfer within the heat exchangers was computed using the conservation of energy for incompressible fluids within a pipe:

$$\rho A C_p u \boldsymbol{e_t} \cdot \boldsymbol{\nabla_t} T = \boldsymbol{\nabla_t} \cdot (Ak \boldsymbol{\nabla_t} T) + \frac{1}{2} f_d \frac{\rho}{d_h} |u| u^2 + Q_{wall}, \tag{2.6}$$

where T is the temperature of the entire pipe cross section $[K]$.

Finally, Q_{wall} within Eq. 2.6 accounts for the heat exchange through the HDPE tube with the concrete $[W/m]$:

$$Q_{wall} = h_{eff}(T_{ext} - T), \tag{2.7}$$

$$h_{eff} = \frac{2\pi}{\frac{1}{r_0 h_{int}} + \frac{1}{r_1 h_{ext}} + \frac{\ln(\frac{r_1}{r_0})}{k_{HDPE}}}, \tag{2.8}$$

where T_{ext} is the exterior temperature $[K]$, r_0 is the inner radius of the heat exchanger tube $[m]$, r_1 is the outer radius of the tube wall $[m]$, k_{HDPE} is the thermal conductivity of the HDPE heat exchanger tube, and h_{int} and h_{ext} are the film heat transfer coefficients determined by the Nusselt number of the flow (which depends on the Reynolds number, Prandtl number, and f_d).

Parametric combinations were compared by quantifying heat rejected (heat transferred) (W/m) (Eq. 2.9). This quantification of performance encourages a practical understanding of the parameter-operation relationship.

$$Q_{rejected} = c_w \rho_w q_{in} \frac{(T_{inlet} - T_{outlet})}{L_{pile}}, \tag{2.9}$$

where c_w is the specific heat capacity of the working fluid $[J/(kg * K)]$, ρ_w is the density of the working fluid $[kg/m^3]$, q_{in} is the flow rate $[m^3/s]$, and L_{pile} is the length of the energy pile $[m]$.

2.5 Summary of test site

The calibration of the model was performed using temperature data collected by (Murphy et al., 2015) from a group of energy piles installed beneath a 1-story building on the

USAFA campus in Colorado Springs, CO. Specifically, the spatial and temporal variations in foundation and subsurface temperatures were used to calibrate the heat transfer model implemented in COMSOL and presented in this paper. Each cylindrical energy pile had a diameter of 0.61 m (meters), a length of 15.2 m, and contained a W-shaped heat exchanger with one inlet and one outlet (Fig. 2.2b). The inlet and outlet were placed 90^o apart and the heat exchangers were attached to the inside of the rebar cage - approximately 0.46 m in diameter. These heat exchangers were 19 mm diameter HDPE tubes with 3 mm wall thicknesses. The installed energy piles included embedded instrumentation to infer the change in temperature and thermal axial strain at several depths. Further, the soil surrounding the energy piles included an array of thermistors at different depths and radial locations. These thermistors had a precision of 0.1^oC and were used to infer the heat transfer away from the energy piles. A layout of the energy pile group supporting the 1-story building, as well as the surrounding array of observational equipment is shown in Fig. 2.3b. The network of strain and temperature monitors collected data at five-minute intervals during a Thermal Response Test (TRT) carried out during the summer of 2013. Murphy et al. (2015) used these observations experimentally to characterize thermo-mechanical response within the energy piles. The current study used the field-collected data to construct, calibrate, and validate a numerical model. Following calibration/validation, the model was used to gain insight into energy pile performance with respect to construction specifications (concrete cover, shank distance, pile spacing).

2.6 Model details

COMSOL model geometry (Fig. 2.2a) matches the experimental group of piles shown in Fig. 2.3 and described in Sec. 2.5. The soil block surrounding the piles measured 40 m x 21 m x 22.5 mm and ensured 15 m between the pile and any subsurface boundary conditions,

thus avoiding unnecessary boundary condition interaction.

The model geometry was constructed within COMSOL software. COMSOL encourages parameterization by allowing the user to build geometry based on variables (e.g. concrete cover, shank distance, pile diameter, pile length, etc.). In this way, multiple simulations can be run for a specific variable.

2.7 Material Properties

Material properties were assigned to their respective domains to simulate reality as closely as possible. Properties of the stratified soil block, concrete piles, HDPE heat exchanger tubes, glycol-water working fluid, and atmospheric air are detailed in Table 2.1. Material densities reported by Murphy et al. (2015) were assigned to respective materials within the model, while remaining properties required for the heat transfer model were adjusted during calibration, as detailed in Section 2.10. These properties included thermal conductivity, specific heat capacity, and porosity.

2.8 Boundary conditions

All boundary conditions were imposed on the model using data collected from the field experiment detailed by Murphy et al. (2015). These observation based boundary conditions were applied as variable interpolation functions.

Atmospheric temperature observations (Fig. 2.4) were applied to the top surface of the model (representing the ground surface) with a transient Dirichlet temperature boundary condition. A thin layer of insulating air (50 mm) was used as a buffer between the temperature boundary condition and the soil/concrete slab. This buffer more accurately reflected

reality and avoided error resulting from direct application of atmospheric temperature to soil surface.

Subsurface temperature gradient measurements were applied to the boundaries of the soil block with a variable (with depth) Dirichlet temperature boundary condition. Two additional Dirichlet boundary conditions were applied to the inlet of the heat exchanger tubes: transient temperature and flow. Inlet temperatures collected from the field (Fig. 2.5) were directly applied to the boundary condition within the model. The flow conditions within the heat exchangers were variable with time, operating at 106 ml/s for the first 500 hours, followed by 1,200 hours of 0 ml/s.

Finally, an adiabatic symmetric boundary condition was used to model only two of the four piles active during the TRT (Fig. 2.2b). The adiabatic boundary condition decreased the computational cost and resulted in a higher density mesh.

2.9 Convergence study

Careful attention was paid to building the equilateral triangular finite-element mesh for the numerical USAFA energy pile model. The distribution of elements was optimized using a convergence study that ensured a sufficient level of accuracy while minimizing computational time and resources. The global domain encompassing the 19,000 m^3 stratified soil block, two 15.2 m long x 0.61 m diameter concrete energy piles, a 50 mm thick concrete slab, and a 50 mm-thick layer of air was partitioned into four respective subdomains. A convergence study was first performed on the concrete pile subdomain. Maximum pile temperature was selected as the characteristic output parameter. It was clear that these piles required a high density of elements to closely approximate temperature distribution. Minimum element

size, growth rate, and resolution were manipulated until the output parameter reached $\Delta T_{max} < 0.1^oC$ (corresponding to a 0.33% change in ^oC) between mesh refinement steps. Following the conclusion of the concrete pile mesh refinement, the soil block mesh was studied. Again, maximum soil block temperature was used as the characteristic output parameter. Element growth rate and minimum element size were manipulated until the output parameter reached $\Delta T_{max} < 0.1^oC$. Lastly, the air and concrete slab domains were not considered during the mesh refinement study, because the purpose of these domains was strictly for insulation. Therefore, these meshes were reduced to the minimum number of elements necessary to achieve the observed insulating characteristics during the calibration phase. The final average equilateral element quality for the global domain was 0.81 for $\approx 600,000$ elements, which ensured that the elements were distributed in a way that captured the heat transfer in the most efficient manner possible without sacrificing solution accuracy. The refined mesh is shown in Fig. 2.6.

2.10 Calibration and validation

The preliminary calibration of the model was detailed in Caulk et al. (2014). The final calibration presented here yields a model with improved accuracy compared to the preliminary calibration due primarily to the improved mesh (described in Section 2.9) and further discretization of soil porosities. Prior to full calibration, model heat exchanger outlet fluid temperatures were compared to field outlet temperatures. These values matched very well, leading to a full calibration (Fig. 2.5). Temperature field data stamped with time and location (x,y,z) were collected at five minute intervals along the length of the in-situ energy piles and nearby boreholes for a duration of 1,700 hours (71 days) (exact locations are shown in Fig. 2.3). First, for 500 hrs of active energy pile heat rejection, followed by 1,200 hrs of cooling observation. Calibration was performed using in-situ temperatures during active heat rejection (time=214 and 500 hours). Validation was performed using the in-situ

temperatures following cooling (time=1,700 hours).

Field data along the length of Foundation 4, Borehole 4 (BH4), and Borehole 6 (BH6) were compared to temperature data output by the COMSOL model as shown in Fig. 2.7. BH4 & BH6 were selected due to diversity of distance from Foundation 4 and exposure/non-exposure to atmospheric conditions. BH4 represents several depths of observation beneath the concrete slab close to Foundation 4 (1.22m), while BH6 represents several depths of observation exposed to atmospheric conditions and further from Foundation 4 (2.44m).

The comparison of field data to model output at the aforementioned locations *during active heat rejection* dictated the calibration of thermal conductivities, heat capacities, and porosities of individual soil layers. These values were adjusted to minimize the differences between the model temperature output and the field temperature observations. Soil and rock densities were not altered from those reported by Murphy et al. (2015). Model output compared to field measurements at the end of cooling were then used for model validation. Final calibrated properties agree with values published in Murphy et al. (2015) (see Table 2.1) and generally accepted heat capacity (Eppelbaum et al., 2014) and porosity values for sandy soil and sandstone rock.

The final calibrated and validated model results are shown in Fig. 2.7 and Fig. 2.8. The calibrated model matched the experimental data well; the RMSE for Foundation 4, BH4, and BH6 were 0.97, 0.67, and 0.82^oC, respectively. Model output error was calculated between the model predicted and measured temperatures as follows (see Tables 2.2, 2.3, and 2.4):

$$error = abs(((measured - predicted)/measured))X100\% \tag{2.10}$$

Greater error was observed at the shallow depths of 0.6-1.8 m and the long duration of 1700 hours. These higher errors at shallow depths may be a result of surface phenomena that was not accounted for within this model (e.g. rain, wind, solar radiation). In comparison, BH4 remained protected by a concrete slab throughout the duration of the experiment and exhibited higher accuracy temperature predictions after 500 hrs at the surface compared to BH6, which was exposed to the atmosphere for the duration of the TRT. Error associated with the validated long duration of 1,700 hours can be attributed to model propagated error.

2.11 Results and discussion

2.11.1 Effects of concrete cover and shank distance

Concrete cover and shank distance are both construction specifications that affect the performance of an energy pile (Caulk and Ghazanfari, 2015). Concrete cover is defined as the minimum distance between the heat exchanger tube and the outer edge of the concrete pile (Fig. 2.1). This construction/design specification is generally controlled by the necessity to protect reinforcing steel, provide thermal insulation, and maintain stresses. Energy pile design should consider concrete cover as an important piece of the design since heat exchangers are fixed to the inside of the reinforcing steel cage.

Similar to concrete cover, shank distance is a construction specification that is easily modified. Shank distance describes the width of the downwards U of a heat exchanger as shown in Figures 2.1 and 2.9. These simple specifications can impact the performance of an energy pile. Therefore, this study used a calibrated numerical model of a group of energy piles to investigate the impact of concrete cover and shank distance on energy pile performance.

Table 2.1: Calibrated material properties of COMSOL model

	Property			
Material	Thermal Conductivity $[W/(m*K)]$	Specific Heat Capacity $[J/(kg*K)]$	Density $[kg/m^3]$	Porosity
Sandy Fill (0-1 m)	1.1	860	1875	0.2
Dense Sand (1-2 m)	0.75	935	1957	0.15
Sandstone (2-12.5 m)	1.7	900	2200	0.1
Dense Sandstone (12.5-22.5 m)	1.8	910	2300	0.05
Concrete	1.4	960	2400	-
Glycol/water	0.58	3267	1.008	-
Air	0.023	1	1.2	-
HDPE	0.48	-	-	-

Table 2.2: Foundation 4 model error with respect to field measurements for calibration and validation (three time periods and eight depths)

%Error		Depth (m)								Average
Foundation 4		0.8	2.6	5.9	7.6	9.1	10.9	12.9	14.6	
Time (hours)	214 (calib.)	3.8	0.33	3.75	4.57	0.30	0.95	0.87	3.04	2.20
	500 (calib.)	0.85	1.52	1.19	1.98	2.28	1.12	1.43	1.20	1.45
	1,700 (valid.)	20.62	8.58	1.89	3.02	3.58	4.81	4.65	3.46	6.32
Average		8.43	3.48	2.28	3.19	2.06	2.30	2.32	2.57	

Table 2.3: Borehole 4 model error with respect to field measurements for calibration and validation (three time periods and six depths)

%Error		Depth (m)						Average
BH 4		0.6	1.8	3.7	7.3	9.8	14.6	
Time (hours)	214 (calib.)	3.15	2.97	1.81	2.83	0.02	7.15	2.99
	500 (calib.)	0.79	1.12	4.27	0.07	4.36	3.33	2.33
	1,700 (valid.)	6.97	8.48	6.67	1.52	3.52	3.14	5.05
Average		3.64	4.19	4.25	1.47	2.63	4.54	

Table 2.4: Borehole 6 model output error with respect to field measurements for calibration and validation (three time periods and six depths)

%Error		Depth (m)						Average
BH 6		0.6	1.8	3.7	7.3	9.8	14.6	
Time (hours)	214 (calib.)	5.87	3.69	2.7	0.18	0.52	1.10	2.34
	500 (calib.)	12.13	9.94	1.51	0.53	0.46	3.59	4.70
	1,700 (valid.)	7.75	10.17	6.02	1.22	3.56	3.50	5.37
Average		8.58	7.94	3.41	0.65	1.52	2.73	

It would be expected that these specifications are optimized upon even distribution throughout the pile (i.e. the tubes are equidistant from their direct neighbors)(Fig. 2.9). Even heat exchanger distribution yields an evenly heated pile cross-section which leads to the maximum energy pile performance (Eq. 2.9). This study attempted to verify this assumption numerically, and quantify the performance increase/decrease with respect to concrete cover and shank distance.

The model was simulated for 500 hours and was constrained by the same boundary conditions as described in Sec. 2.8 and Sec. 2.10. Simulations were performed for a range of concrete covers (0.04-0.145 m) and shank distances (0.10-0.45 m). The final $\Delta T(500hrs)$ was used with Eq. 2.9 to determine the quantity of heat rejected for each parameter combination as shown in Fig. 2.10.

Concrete cover plays an important role in total heat rejected. For a shank distance of 0.35 m, an increase of concrete cover from 0.04 to 0.11 m yielded a 9.7 % decrease in heat rejected. These results confirm findings in the literature (Cecinato and Loveridge, 2015; Caulk and Ghazanfari, 2015); as concrete cover is increased, heat rejected is decreased. Shank distance also contributes to final energy pile performance. For a concrete cover of 0.04 m, shank distance increased pile heat rejected by 8.3 % (0.1-0.325 m shank distance, where 0.325 m corresponds to an even heat exchanger layout). However, beyond the shank distance associated with even heat exchanger layout, the amount of heat rejected decreased due to the redevelopment of an uneven heat exchanger layout.

These results verify the model by proving its sensitivity to small changes in cross-sectional heat exchanger configuration. Evenly spaced heat exchangers yielded the best

energy pile performance due to an evenly heated cross-section (Fig. 2.10), while even small changes to heat exchanger layout reduced the energy pile performance due to an unevenly heated cross-section. This model verification enabled the investigation of cross-sectional temperature distribution and its role in the approximation of thermal axial stresses.

2.11.2 Cross-sectional temperature distribution

The cross-sectional temperature distribution of an energy pile plays a key role in thermal axial stress estimation via strain/temperature gages. The approximation of in-situ thermal axial stress relies on the temperature and strain at the location of the gage as follows:

$$\sigma_T = E(\epsilon_T - \alpha_c \Delta T), \tag{2.11}$$

where σ_T is the thermal stress [MPa] as a function of Young's modulus (E) [MPa], thermal strain (ϵ_T), coefficient of linear expansion of concrete (α_c) [$\mu\epsilon/^oC$], and temperature (ΔT) [^oC]. Positive σ_T and ϵ_T values indicate compression as a result of heating expansion, which means α_c must be defined as a negative value to accommodate for positive ΔT values during heating.

Thermal strains (ϵ_T) reported by Murphy et al. (2015) were computed using the difference between the fluctuating thermal strain caused by the restrained thermal expansion or contraction of the concrete (ϵ_i) and the initial strain due to the building load (ϵ_0). Thermal axial stresses were then calculated using Eq. 2.11, which relies on ϵ_T and ΔT at the point of the gage. Murphy et al. (2015) extended the study by evaluating the thermal axial strain as a function of ΔT at several depths, which enabled the estimation of a mobilized coefficient of thermal expansion, α_{mob} [$\mu\epsilon/^oC$] with depth. Since α_{mob} is a function of ΔT and depth, the study presented in this paper estimated theoretical thermal axial stresses

using the following equation:

$$\sigma_{T,theo} = E((\alpha_{conc,free} - \alpha_{mob})\Delta T) \tag{2.12}$$

where $\sigma_{T,theo}$ is the theoretically determined thermal axial stress [MPa] and α_{free} is the coefficient of free expansion $[\mu\epsilon/^oC]$.

Since the cross-sectional temperature distribution can vary by up to 4^oC (Loveridge and Powrie, 2013), ϵ_T and ΔT at the location of the gage may contribute to an under/overestimated thermal stress. Therefore, this study used a calibrated model of a group of energy piles to demonstrate the evolution of cross-sectional temperature and stress distribution. For this analysis, the model was simulated for 500 hours and was constrained by the same boundary conditions as described in Sec. 2.8 and Sec. 2.10. Probes were used to extract cross-sectional temperatures within the model (Fig. 2.9). Time and location stamped temperatures were then post-processed to compute theoretical cross-sectional thermal stresses (Eq. 2.12).

Fig. 2.11 shows the evolution of cross-sectional temperature/thermal axial stress distribution with time for an even heat exchanger layout (Fig. 2.9a) at 7.6m depth. At 10 hours, the distribution was relatively even, but by 250 hours the core of the pile stabilized to 4^oC above the strain gage. The corresponding thermal axial stress difference between the core and the strain gage stabilized to 0.88 MPa after 250 hours. This difference corresponds to a thermal axial stress increase of 20% between the strain gage and the core for the duration of the TRT.

The temperature distribution with respect to the primary and secondary cross-sections (Fig. 2.9a) varied depending on the shank distance and concrete cover. As expected, the

evenly distributed heat exchangers (Fig. 2.9a) yielded the most evenly distributed temperature/thermal axial stress; cross-sectional temperatures and stresses varied by $\approx 0.3^oC$ and 0.06 MPa (Fig. 2.11) around the perimeter, respectively. Conversely, the extreme shank distances of 0.1 m and 0.45 m (Fig. 2.9b&c) yielded the least evenly distributed temperature/thermal stress; cross-sectional temperatures and stresses varied by $\approx 8^oC$ and 1.71 MPa around the perimeter (Fig. 2.12a and 2.12b). Furthermore, these extreme combinations also exhibited thermal axial stress differences of $\approx$ 1.15 MPa between the strain gage and the core.

These results also shed light on energy pile performance. The energy pile performance corresponding to the parameter combinations used to build Figures 2.11, 2.12a, and 2.12b are shown in Fig. 2.10. The uneven temperature distributions of Fig. 2.12a & 2.12b correspond to a decrease of heat rejected by $\approx$ 8%. Conclusively, the evenly spaced heat exchanger layout corresponds to higher energy pile performance.

2.11.3 Effect of pile spacing

Pile spacing may be dictated by structural design, geotechnical investigations, or foundation design. Therefore, this design specification may not be as simple to manipulate as concrete cover or shank distance. However, this study used the calibrated/validated model to quantify the relationship between pile spacing and energy pile performance. Results from this exercise were used to support findings in the literature and further verify the model.

The model was simulated for 500 hours and was constrained by the same boundary conditions as described in Sec. 2.8 and Sec. 2.10. Simulations were performed for a range of pile spacings (0.5-16 m). For each value of pile spacing, the soil block was adjusted to maintain the same distance between the pile and the boundary conditions. This boundary

adjustment isolated the pile spacing as the only parameter that contributed to changes of heat rejected. The final $\Delta T(500hrs)$ was used with Eq. 2.9 to determine the performance of each pile spacing.

Fig. 2.13 exhibits the performance of the energy piles with respect to pile spacing. As expected, the heat rejected increases with increased pile spacing. An increase of 4 m (1-5 m) increased heat rejected by 21.7%. As the pile spacing increases, the thermal gradient between the pile and surrounding soils remains greater for a longer period of time, resulting in more heat rejected. Conversely, the thermal gradient decreases as the piles approach one another. This decreased thermal gradient is due to the heated soil nearby the neighboring pile resulting in a lower thermal gradient, lower heat rejected, and lower pile performance.

These results further verify the model and support findings from the literature. Morino and Oka (1994) used a validated numerical model to investigate the temperature distribution surrounding a steel pile. The study concluded that the soil temperature remained undisturbed 3 m from the energy pile. Fig. 2.13 shows that performance plateaus for two piles spaced $\approx$6 m, supporting the conclusions drawn by Morino and Oka (1994).

2.12 Conclusions

The calibration, validation, and parameterization of a full-scale geothermal energy pile model was performed using advanced finite element analysis software and HPC. Final results from the parametric study verified the model and provided insight into the relationship between model parameters and energy pile performance. The validated model was also used to analyze the evolution of the cross-sectional temperature/thermal stress.

Full calibration of the three-dimensional model required detailed boundary conditions, discretized soil layers, and extensive field data. All boundary conditions were variable with time or space, and were imported directly from the field data (atmospheric temperatures, subsurface temperature gradients, inlet temperatures, etc.) Several layers of soil were used to calibrate the model output to the field data. Each soil layer was identified by several unique material properties, namely, heat capacity, thermal conductivity, and porosity. These properties were carefully calibrated using time series temperature data at nine depths within the concrete energy pile and six depths within the surrounding soils.

The amount of heat rejected from an energy pile into surrounding soils with respect to geometrical parameters was quantified by model parameterization. Energy pile performance was evaluated as a function of concrete cover, shank distance, and pile spacing. This parametric sweep verified the original assumption that the optimal heat exchanger configuration (combination of concrete cover and shank distance) is the configuration that maintains equal distances between heat exchanger pipes (in cross-section view). Additionally, this parametric sweep quantified the loss of performance as pipes become less evenly distributed. A change of heat exchanger configuration can alter performance by up to 9%. Furthermore, the parametric sweep verified the sensitivity of the model to cross-sectional temperature distributions.

Upon validation of the model, the evolution of the cross-sectional temperature/thermal axial stress distribution during a heating cycle was investigated. The result of this investigation demonstrated the under/over estimation of thermal axial stress reported by field experiments. In particular, the USAFA experiment used to calibrate the model was reliant on embedded strain gages to compute thermal stress. These strain gages were attached to the reinforcing cage at the perimeter of each pile. This study showed that the thermal stress

computed at the perimeter of the pile versus the core may vary by up to 1.71 MPa. Furthermore, the heat exchanger layout has a significant impact on temperature/stress distribution. For certain combinations of concrete cover and shank distance, the stress varied by up to 1.15 MPa at different locations around the perimeter of the pile. These results draw several conclusions about the approximation of temperature/thermal axial stress distribution within piles:

1. Cross-sectional thermal axial stress within energy piles is not constant. During heating, the thermal axial stress may be as much as 20% greater at the core of the pile than the reinforcing cage. This should be considered for stress analyses on in-situ energy piles.

2. Evenly distributed heat exchangers distribute temperature and thermal axial stress evenly around the perimeter of the pile, while uneven heat exchanger layouts exhibit extreme temperature/thermal axial stress variance across the core and around the perimeter of the pile.

3. The performance of an energy pile depends strongly on its cross sectional temperature distribution. This study demonstrated that even heat exchanger layouts correspond to even cross-sectional temperature distributions, which correspond to higher energy pile performance.

2.13 Acknowledgements

The authors acknowledge the Vermont Advanced Computing Core, which is supported by NASA (NNX 06AC88G), at the University of Vermont for providing High Performance Computing resources that have contributed to the research results reported within this paper.

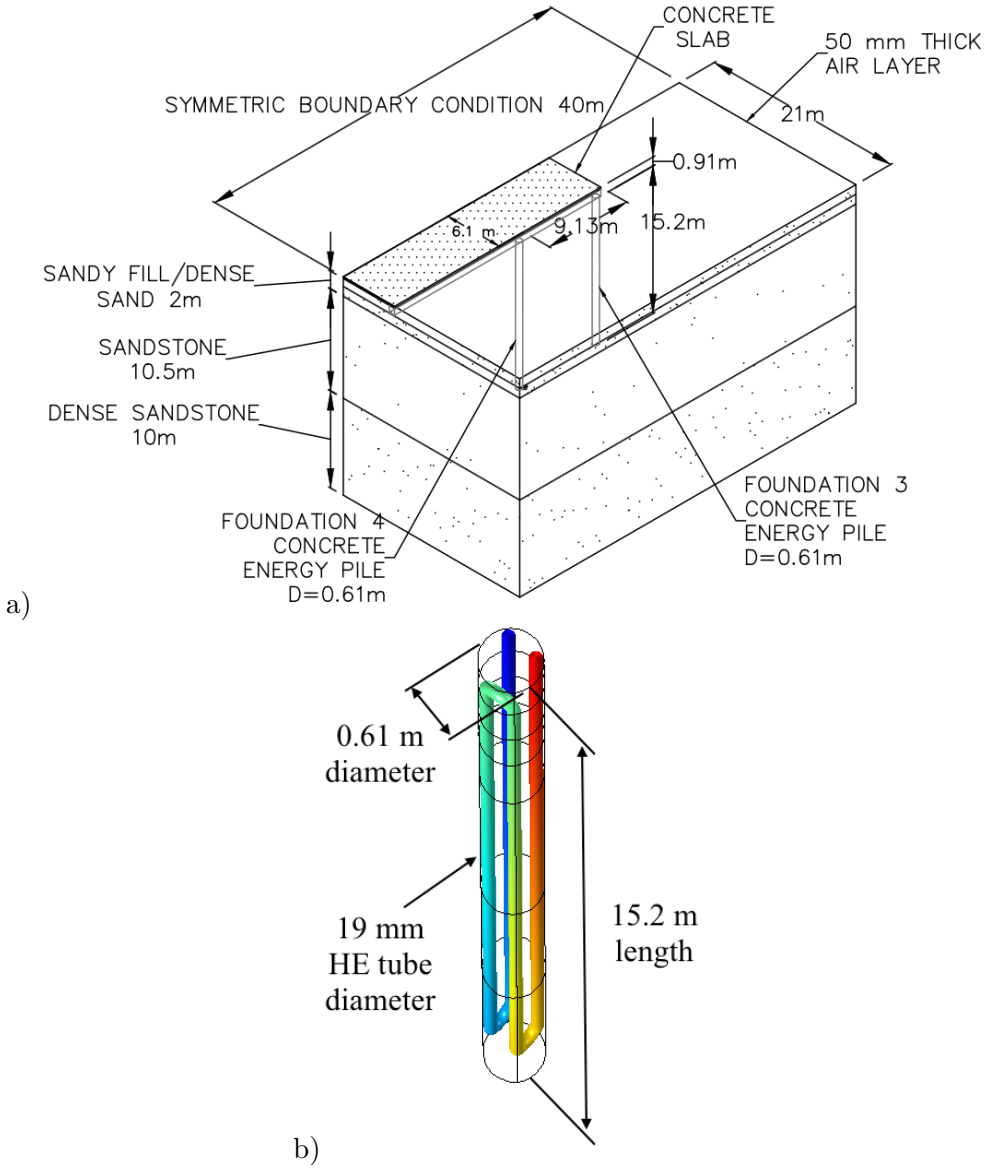

Figure 2.2: COMSOL model geometry a) Full model b) close up of Foundation 4

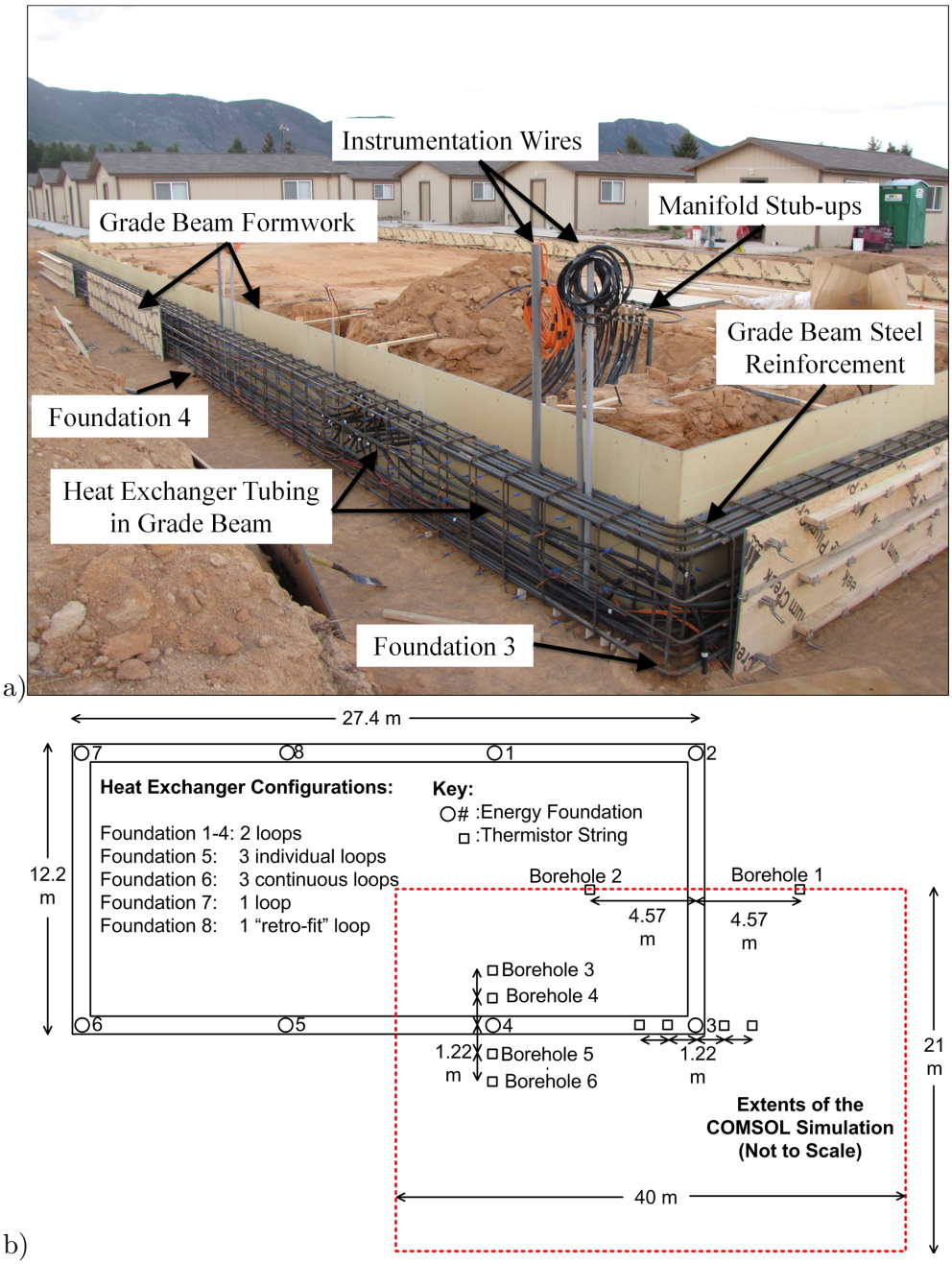

Figure 2.3: USAFA experimental pile group a) construction picture b) plan view (Murphy et al., 2015)

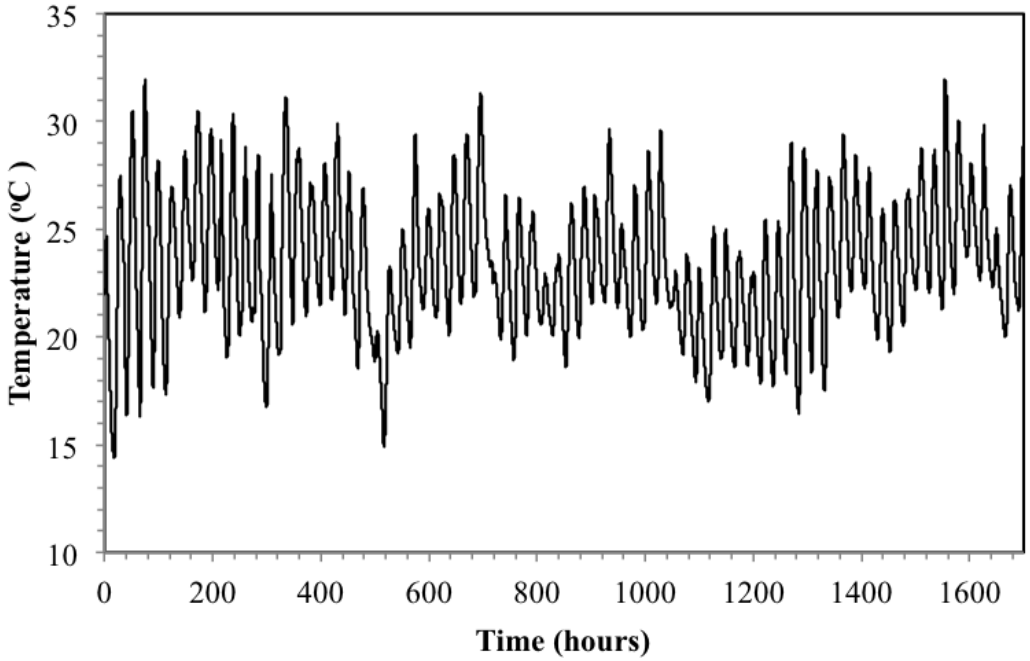

Figure 2.4: Known atmospheric temperature boundary condition applied to the model during the duration of the thermal response test

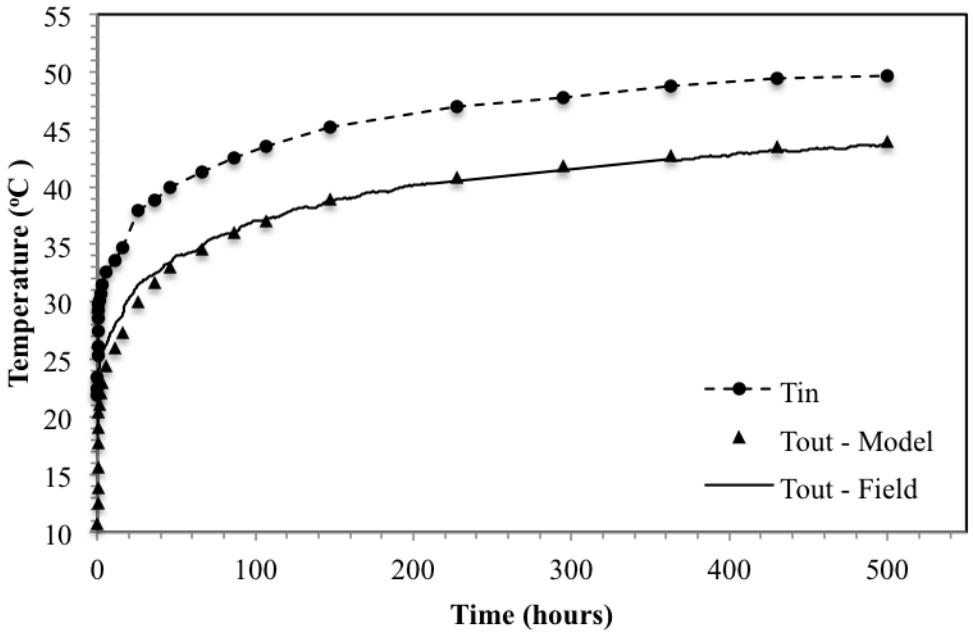

Figure 2.5: Heat exchanger inlet temperature applied as the boundary condition to the model

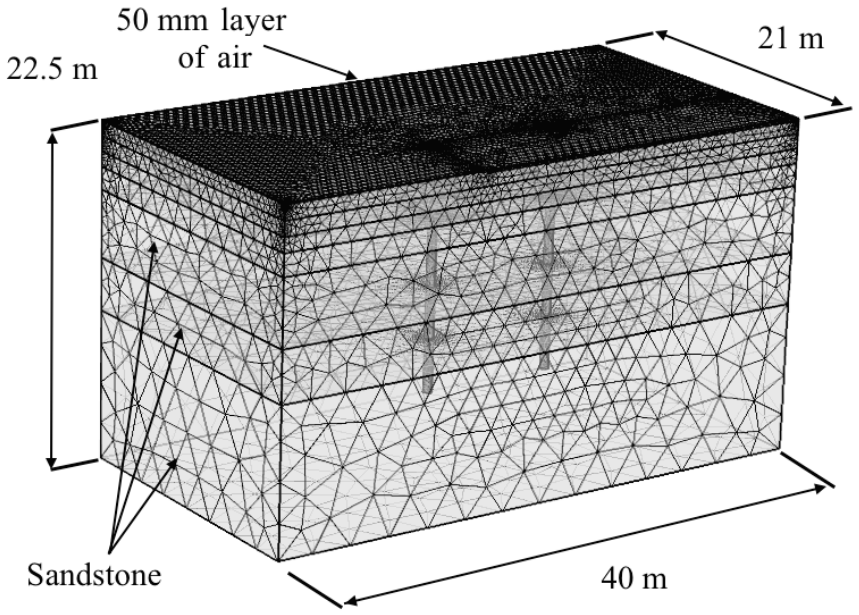

a)

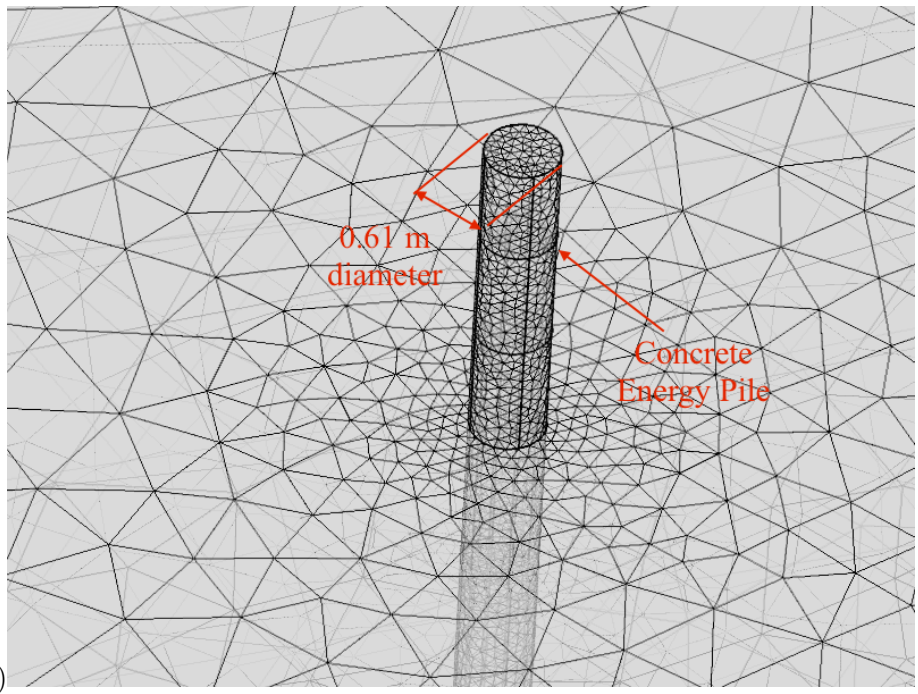

b)

Figure 2.6: Refined COMSOL model mesh a) full view b) close up showing pile and element growth

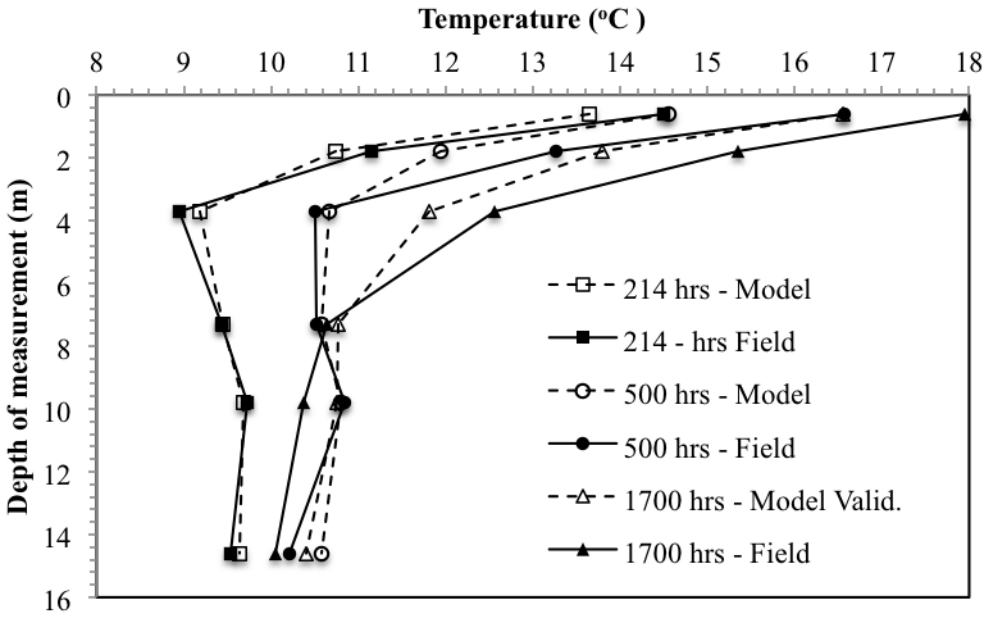

a)

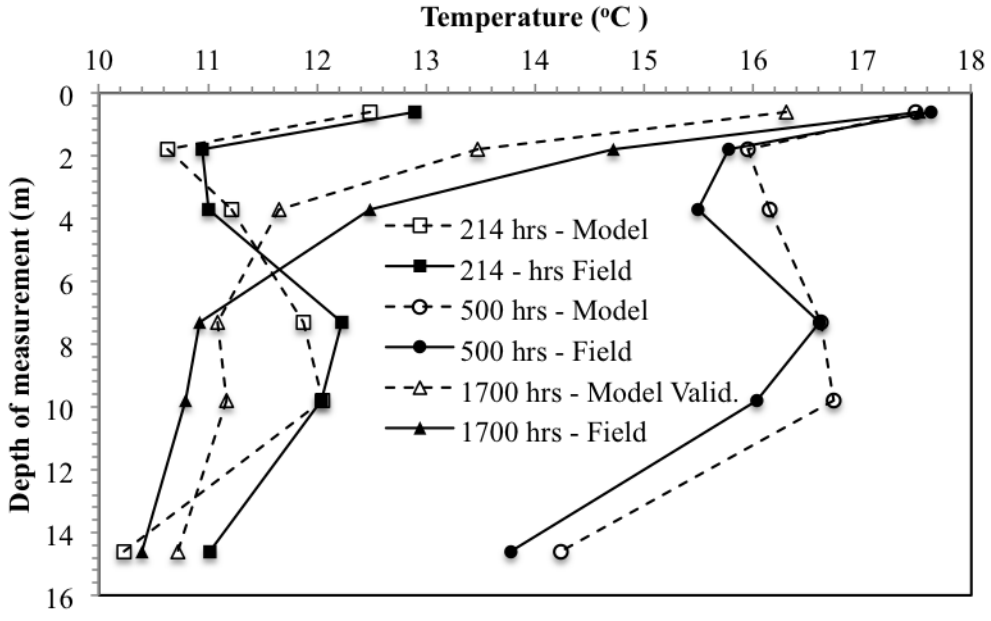

b)

Figure 2.7: Calibrated model comparison for a) Borehole 6 and b) Borehole 4

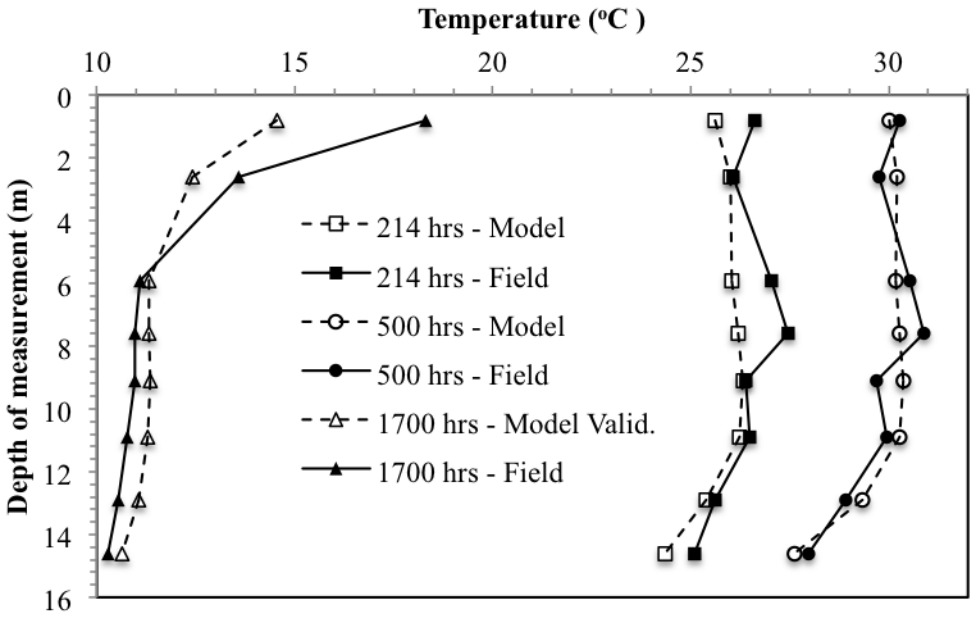

Figure 2.8: Calibrated model temperature comparison for length of Foundation 4 during heating (214 hours) at the end of heating (500 hours) and at the end of cooling observation (1700 hours)

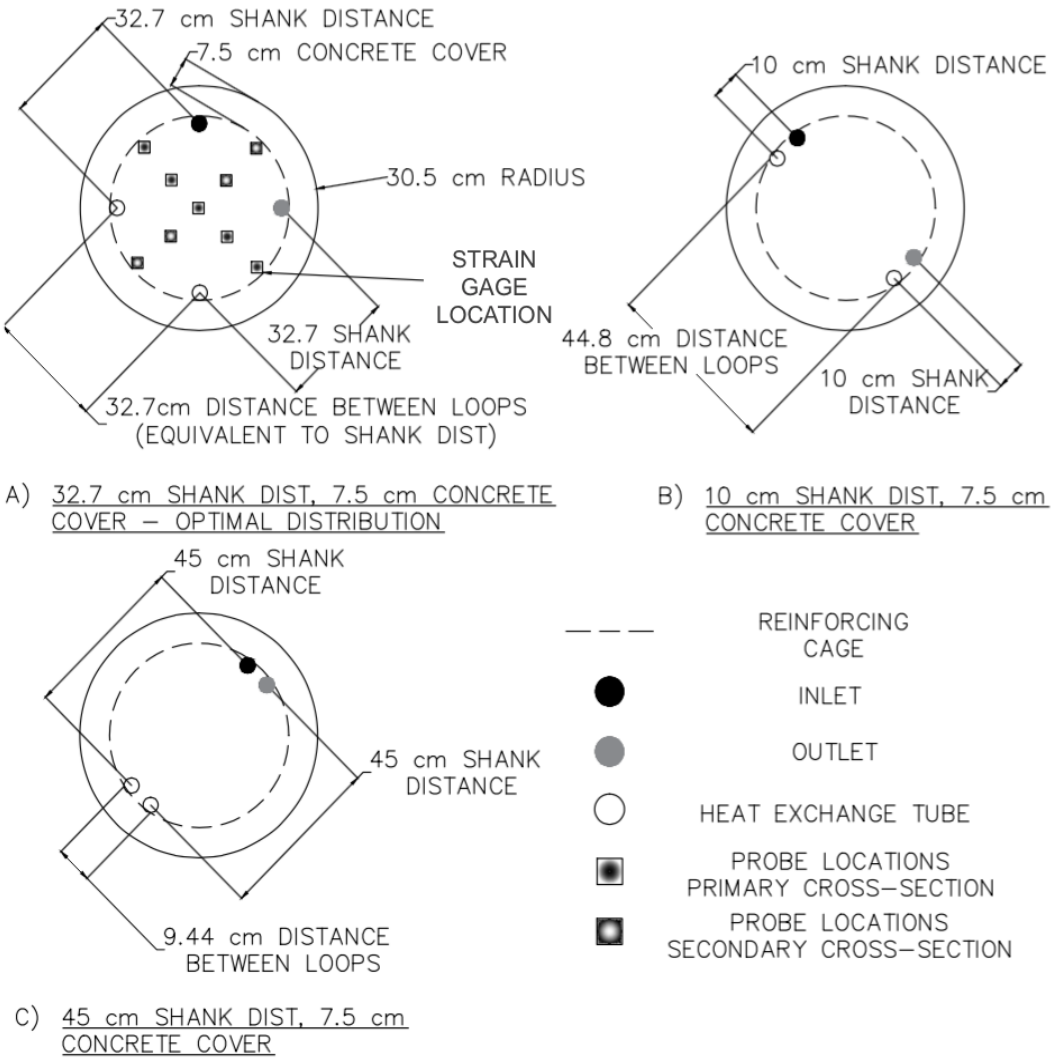

Figure 2.9: Shank distance parameterization and probe locations

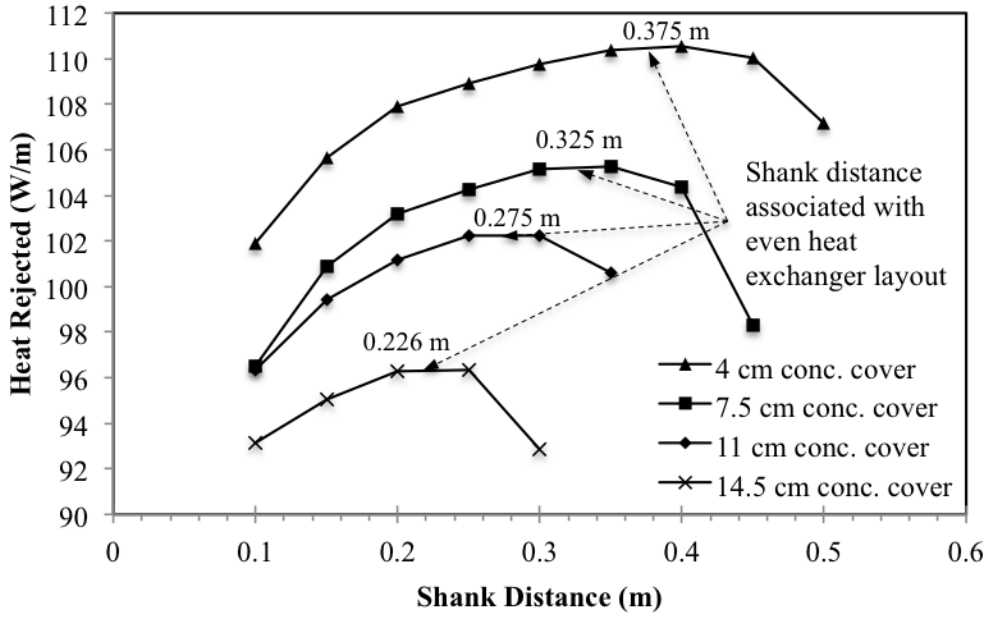

Figure 2.10: Energy pile heat transfer as a function of shank distance and concrete cover

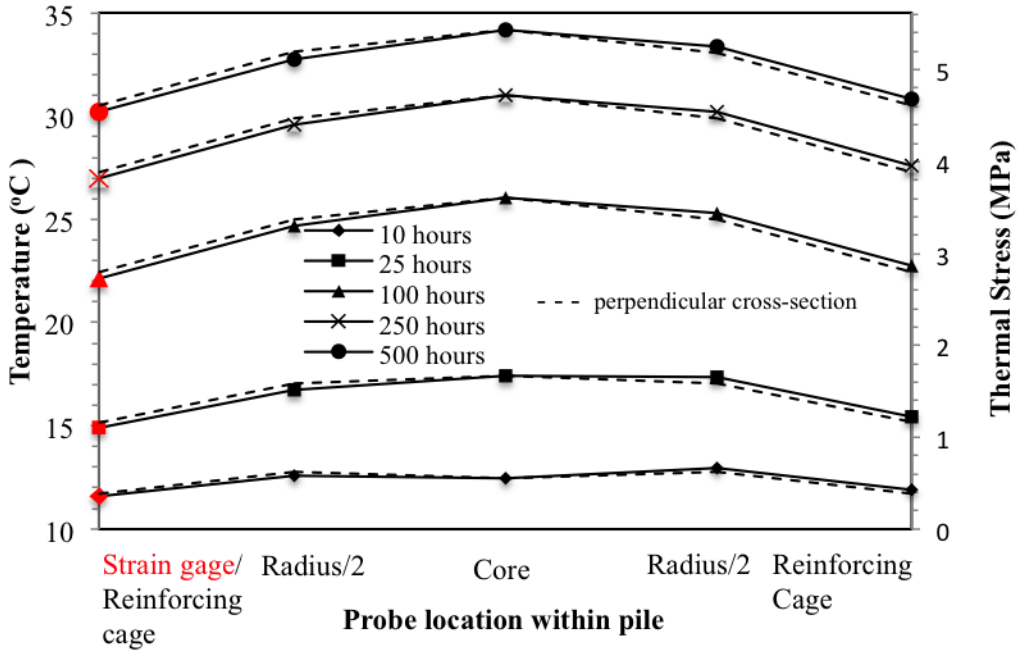

Figure 2.11: Temperature and thermal axial stress distribution for pile cross section at 7.6 m depth and even heat exchanger distribution

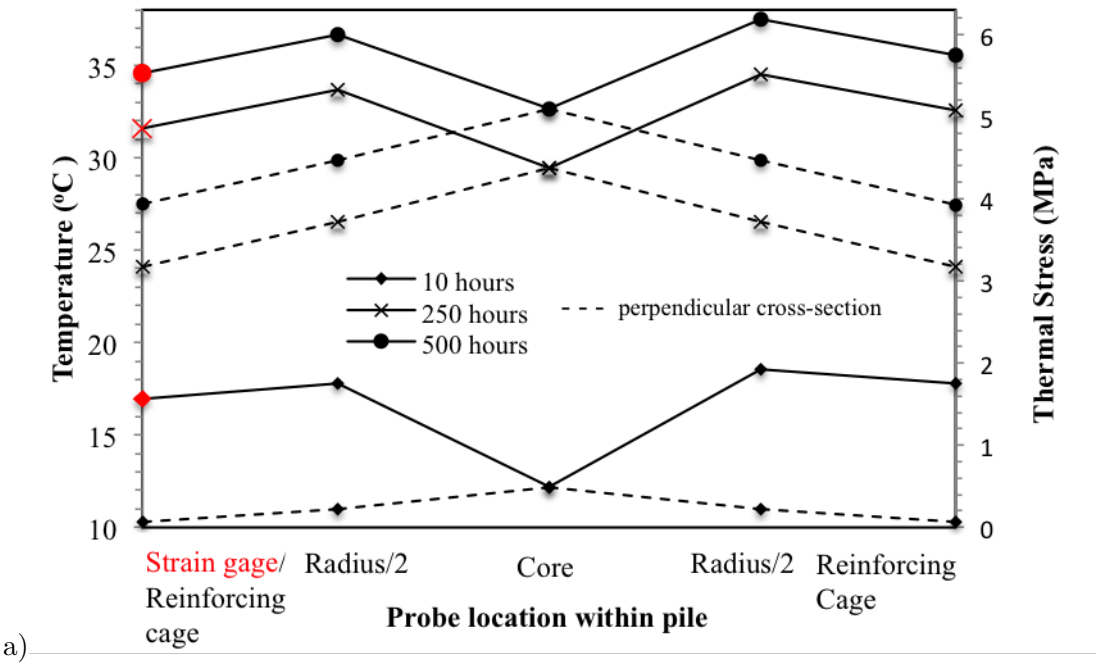

a)

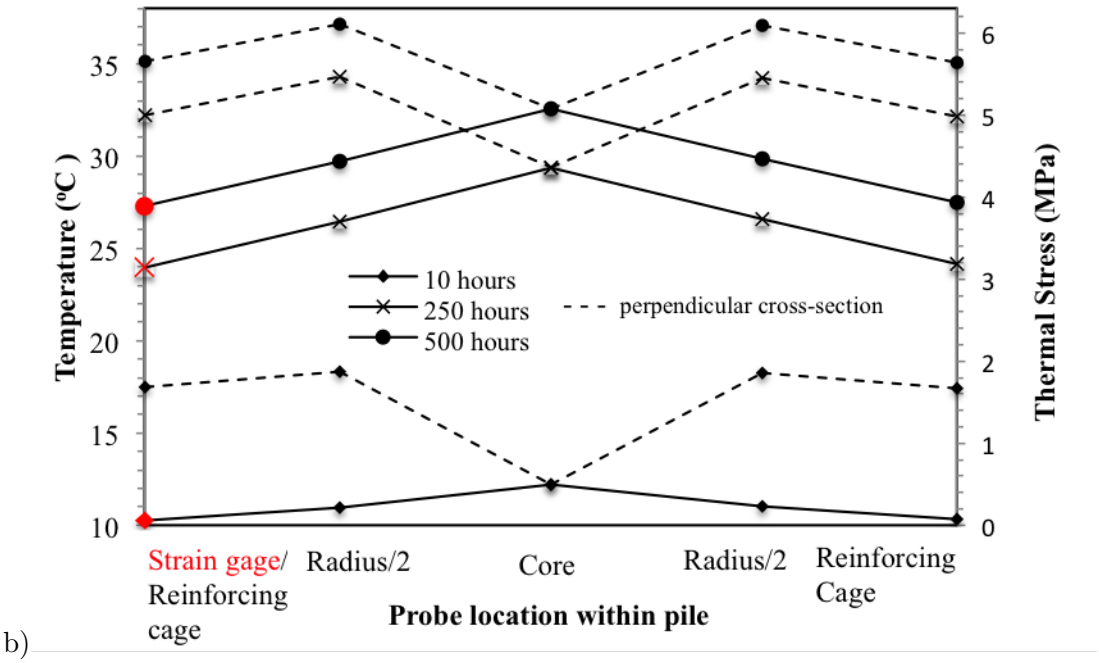

b)

Figure 2.12: Temperature and thermal axial stress distribution for pile cross section at 7.6 m depth and uneven heat exchanger layouts - shank distances of a) 0.10 m and b) 0.45 m (uneven heat exchanger distributions)

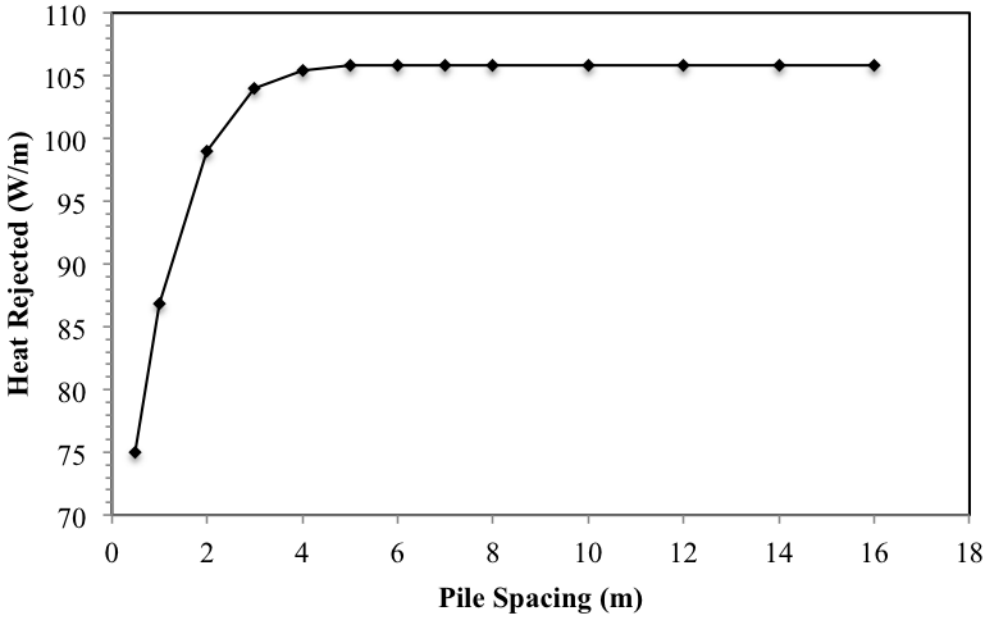

Figure 2.13: Pile performance as a function of pile spacing

Bibliography

Abdelaziz, S. L., Olgun, C. G., and Martin, J. R. (2015). Equivalent energy wave for long-term analysis of ground coupled heat exchangers. *Geothermics*, 53:67–84.

Abdelaziz, S. L., Ozudogru, T. Y., Olgun, C. G., and Martin, J. R. (2014). Multilayer finite line source model for vertical heat exchangers. *Geothermics*, 51:406–416.

Barnard, A. C., Hunt, W. A., Timlake, W. P., and Varley, E. (1966). A theory of fluid flow in compliant tubes. *Biophysical Journal*, 6:717–724.

Bourne-Webb, P., Pereira, J., Bowers, G., Mimouni, T., Loveridge, F., Burlon, S., Olgun, C. G., McCartney, J. S., and Sutman, M. (2014). Design tools for thermoactive geotechnical systems. *DFI Journal: The Journal of the Deep Foundations Institute*, 8(2):121–129.

Bourne-Webb, P. J., Amatya, B., Soga, K., Amis, T., Davidson, C., and Payne, P. (2009). Energy pile test at Lambeth College, London: geotechnical and thermodynamic aspects of pile response to heat cycles. *Geotechnique*, 59(3):237–248.

Brandl, H. (2006). Energy foundations and other thermo-active ground structures. *Géotechnique*, 56(2):81–122.

Caulk, R. and Ghazanfari, E. (2015). Investigation of construction specification effects on energy pile efficiency. In *Proceedings of the International Foundations Conference and Equipment Exposition (IFCEE 2015)*, pages 1648–1657, San Antonio, TX. Mar. 17-21. ASCE.

Caulk, R., McCartney, J., and Ghazanfari, E. (2014). Calibration of a geothermal energy pile model. In *Proceedings of the COMSOL Boston 2014 Conference*, Boston, MA. COMSOL.

Cecinato, F. and Loveridge, F. (2015). Influences on the thermal efficiency of energy piles. *Energy*, 82:1021–1033.

EIA (2011). Annual Energy Review. Technical report, Energy Information Administration.

Eppelbaum, L., Kutasov, I., and Pilchin, A. (2014). Thermal Properties of Rocks and Density of Fluids. In *Applied Geothermics*, Lecture Notes in Earth System Sciences, pages 99–142. Springer-Verlag Berlin Heidelberg, Berlin, Heidelberg.

Gao, J., Zhang, X., Liu, J., Li, K., and Yang, J. (2008). Numerical and experimental

assessment of thermal performance of vertical energy piles: An application. *Applied Energy*, 85(10):901–910.

Gashti, E. H. N., Uotinen, V. M., and Kujala, K. (2014). Numerical modelling of thermal regimes in steel energy pile foundations: A case study. *Energy and Buildings*, 69:165–174.

Ghasemi-Fare, O. and Basu, P. (2013). A practical heat transfer model for geothermal piles. *Energy and Buildings*, 66:470–479.

GSHPA (2012). Thermal Pile Design , Installation and Materials Standards. Technical Report October 2012, Ground Source Heat Pump Association.

Hamada, Y., Saitoh, H., Nakamura, M., Kubota, H., and Ochifuji, K. (2007). Field performance of an energy pile system for space heating. *Energy and Buildings*, 39(5):517–524.

Jalaluddin and Miyara, A. (2014). Performance investigation of multiple-tube ground heat exchangers for ground-source heat pump. *American Journal of Energy Engineering*, 2(5):103–107.

Kaltreider, C., Krarti, M., and McCartney, J. S. (2015). Heat transfer analysis of thermoactive foundations. *Energy and Buildings*, 86:492–501.

Laloui, L., Nuth, M., and Vulliet, L. (2006). Experimental and numerical investigations of the behaviour of a heat exchanger pile. *International Journal for Numerical and Analytical Methods in Geomechanics*, 30:763–781.

Loveridge, F. and Powrie, W. (2012). Performance of piled foundations used as heat exchangers. In *18th International Conference for Soil Mechanics and Geotechnical Engineering*, pages 3371–3374. ICE Geotech Eng.

Loveridge, F. and Powrie, W. (2013). Temperature response functions (G-functions) for single pile heat exchangers. *Energy*, 57:554–564.

McCartney, J. S., Murphy, K. D., and Henry, K. S. (2015). Response of an energy foundation to temperature fluctuations. In *Proceedings of the International Foundations Conference and Equipment Exposition (IFCEE 2015)*, pages 1691–1700, San Antonio, TX. Mar. 17-21. ASCE.

Mimouni, T. and Laloui, L. (2014). Towards a secure basis for the design of geothermal piles. *Acta Geotechnica*, 9(3):355–366.

Morino, K. and Oka, T. (1994). Study on heat exchanged in soil by circulating water in a steel pile. *Energy and Buildings*, 21(1):65–78.

Murphy, K. D. and McCartney, J. S. (2015). Seasonal response of energy foundations during building operation. *Geotechnical and Geological Engineering*, 33(2):343–356.

Murphy, K. D., McCartney, J. S., and Henry, K. S. (2015). Evaluation of thermo-mechanical and thermal behavior of full-scale energy foundations. *Acta Geotechnica*, 10(2):179–195.

Olgun, C. G., Martin, J., Abdelaziz, S., Iovino, P. L., Catalbas, F., Elks, C., Fox, C., and

Gouvin, P. (2012). Field testing of energy piles at Virginia Tech. In *Proceedings from the 37th Annual Conference on Deep Foundations*, Houston, TX.

Ozudogru, T., Olgun, C., and Senol, A. (2014). 3D numerical modeling of vertical geothermal heat exchangers. *Geothermics*, 51:312–324.

Park, H., Lee, S., Yoon, S., and Choi, J. (2013). Evaluation of thermal response and performance of PHC energy pile: Field experiments and numerical simulation. *Applied Energy*, 103:12–24.

Suryatriyastuti, M. E., Mroueh, H., and Burlon, S. (2012). Understanding the temperature-induced mechanical behaviour of energy pile foundations. *Renewable and Sustainable Energy Reviews*, 16:3344–3354.

Wang, W., Regueiro, R. A., and McCartney, J. S. (2014). Coupled axissymmetric thermo-poro-elasto-plastic finite element analysis of energy foundation centrifuge experiments in partially saturated silt. *Geotechnical and Geological Engineering*, 33(2):373–388.

Wood, C. J., Liu, H., and Riffat, S. B. (2009). Use of energy piles in a residential building , and effects on ground temperature and heat pump efficiency. *Geotechnique*, 59(3):287–290.

Chapter 3

Experimental investigation of fracture aperture evolution under coupled thermo-hydro-mechanical-chemical processes encountered in EGS

3.1 Introduction

3.1.1 Literature Review

The success and sustainability of an EGS depends strongly on the permeability of its fracture network. If the permeability decreases, so does the flow rate and the associated electricity generation. Several processes affect the permeability of the system, including thermal, hydrological, mechanical and chemical processes (MIT Report, 2006). These processes interact with one another temporally and contribute to the evolution of permeability within an EGS reservoir during normal operation. Several studies have shown that heat extraction from rock results in thermal contraction (Koh et al., 2011; Ghassemi et al., 2008). This thermal contraction increases aperture width/permeability on the long term and may encourage the

development of internal stresses (Ghassemi et al., 2005). On the other hand, poroelastic effects resulting from fluid injection typically lead to a temporarily increased fracture aperture followed by leak off and the aperture reduction on the long term (Xiong et al., 2013). Numerical simulations that couple thermoporoelastic effects show that thermoelastic effects dominate poroelastic effects over the course of a reservoir's lifespan (Ghassemi et al., 2008; Ghassemi and Zhou, 2011). Thermo-hydro-mechanical processes play important roles in the permeability evolution within an EGS. However, not many studies have investigated the evolution of permeability within an EGS with respect to rock-water chemical interactions in combination with thermo-hydro-mechanical processes within an EGS.

Chemical alterations within a fractured reservoir result in alterations to rock matrix permeability and are strongly coupled to thermal and pressure changes within the system, in other words, mineral precipitation/dissolution may occur as a result of chemical/thermal/pressure imbalances (Ghassemi, 2012). Numerical studies have shown that when the temperature and silica content of a rock are higher than the working fluid, dissolution will increase fracture aperture near the injection well and precipitation decreases fracture aperture at the production well (Xu et al., 2001). Another numerical study performed by Ghassemi and Suresh Kumar (2007) showed that the diffusion of silica into and out of a fracture network decreases the net mass of silica retained within an individual fracture. The study indicates less aperture change by dissolution/precipitation. An improved understanding of the coupled thermo-hydro-mechanical-chemical effects on fracture permeability will help estimate the response of reservoirs to long-term operation and ultimately increase reservoir efficiency and sustainability.

The effects of coupled processes on fracture permeability in EGS reservoirs have been separately investigated to a limited extent (Kohl et al., 1995; Ghassemi and Zhang, 2004,

2006; Ghassemi et al., 2008; Ghassemi and Zhou, 2011; Xiong et al., 2013; Yasuhara and Elsworth, 2006) through numerical, analytical, and semi-analytical studies. Very limited experimental research has, however, been performed to investigate the effects of these processes on fracture permeability in EGS reservoirs. Furthermore, these experimental studies investigated the effect of individual processes rather than coupled processes on fracture permeability (Brace, 1980; Kranz et al., 1979; Barnabe, 1986; Hakami and Larsson, 1996; Oda et al., 2002). Other studies which couple thermo-hydro-mechanical-chemical processes, do so on specimens that do not represent the rock type of EGS (Polak et al., 2004; Singurindy and Berkowitz, 2005). Many studies have focused on the permeability of intact and fractured granite at high temperatures and pressures. Brace (1980) used pulse decay permeametry to measure permeability as a function of effective pressure. They concluded that Darcy's law holds for a range of effective pressures, and that rocks subject to high pressures are nearly impermeable. Kranz et al. (1979) investigated the permeability of whole and jointed Barre Granite using confining pressures up to 200 MPa. They concluded that cycled pore pressures resulted in hysteresis, but this hysteresis diminished at higher confining pressures. Barnabe (1986) also investigated permeability hysteresis for Barre Granite and developed a simple model based on frictional sliding inside the rock. These experiments were performed at pressures greater than those seen in EGS, and temperatures much lower than EGS. Morrow et al. (2001) investigated permeability reduction in granite under hydrothermal conditions. These experiments included the flow of deionized water through crushed/intact granite specimens at EGS temperatures and pressures. They used an SEM to determine that the surfaces of the fractured specimens showed evidence of dissolution. One important observation was the lack of precipitated species following the migration from the heated specimen to the room temperature reservoir. Another geochemistry based granite flow-through experiment was performed by Savage et al. (1992). Although these experiments were constrained by lower temperatures (60-100 ^oC), they employed novel fluid

compositions (stream water and synthetic analogues). The study concluded rock dissolution is a heterogenous process; the effluent gained certain minerals and lost others depending on their reactivity. Another important conclusion was that the most reactive minerals were calcite, feldspar, biotite and quartz. There is an urgent need to study this coupled effect, because the potential for EGS to contribute a significant amount of baseload power to the grid remains untapped until the uncertainty of the resource sustainability is decreased. The research presented here employs an original experimental approach to improve the limited understanding of coupled processes in EGS reservoirs.

3.1.2 Objective

The objective of this research was to develop an experimental methodology that can analyze fracture aperture evolution with respect to coupled thermo-hydro-mechanical-chemical processes. The motivation for the development of this type of experimental methodology stems from the lack of published literature regarding fracture aperture evolution at EGS conditions. As discussed in Sec. 3.1.1, there exists a pressing need for the understanding of granite-water interactions on fracture permeability at EGS conditions. Specifically, there remains a gap in the literature addressing the dissolution of minerals within EGS. Fracture surface asperities initially prop the fracture open (Fig. 3.1), but upon introduction to deionized water, the asperities dissolve and the fracture aperture closes, resulting in decreased permeability. The methods developed to support this hypothesis are described in Sec. 3.4. However, the preliminary work required to study fracture aperture evolution within granite EGS involved intensive specimen characterization, and is therefore covered first in Sec. 3.2.

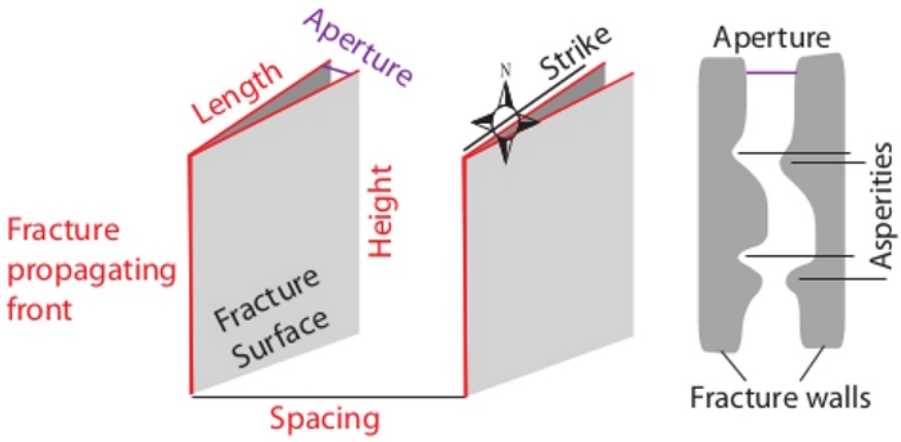

Figure 3.1: Diagram of rock fracture measurements
Source: GeoExPro Magazine

3.2 Block selection and geological history

In order to experimentally study the evolution of fracture apertures within granite based EGS, the specimen must be carefully selected. The ideal specimen would be extracted from a granite reservoir several kilometers beneath the Earth's surface. However, the cost of extracting these rocks is enormous. For this reason, this study investigated alternative specimens. A local opportunity presented itself at the Rock of Ages Barre Granite Quarry located in Barre, Vermont, USA. The quarry originated as an intrusive deposit (pluton) during the Devonian age ($\approx 420 Mya$). This granodiorite pluton was a massive magma chamber that cooled slowly several kilometers beneath the Earth's surface. Therefore, for all intents and purposes of this study, granite specimens extracted from the Barre Granite quarry are representative of a granite EGS similar to Soultz-sous-Forets in France. Furthermore, the quarry by nature exposes unweathered rock from deep within the formation. Thus, the specimens extracted from the quarry are also unweathered like the granite within an EGS.

3.3 Block Characterization

The block of Barre Granite used for specimen creation was first characterized to identify proper coring and fracturing orientations. Granite generally exhibits isotropy with respect to material properties. However, there are three distinct planes that are used to characterize granite: the rift, the grain, and the hardway (Fitz Osbourne, 1935). The rift is the plane along which granite will fracture with greatest ease and is typically controlled by foliation within the rock. Additionally, the rift is characterized by higher permeability than the grain or the hardway. The grain is oriented at a right angle to the rift and is generally visible to the naked eye. Finally, the hardway is oriented at right angles to both the rift and the grain. This plan breaks with greater difficulty and can be identified by a much coarser mineral distribution.

Nasseri et al. (2010) studied the orientation of micro cracks in a Barre Granite specimen using ultrasonic velocities. The study found a strong concentration of micro cracks along the plane of greatest weakness (rift). Since in-situ granite should fracture perpendicular to the plane of greatest weakness, the study presented here attempted to identify the rift plane before coring the block and fracturing the experimental specimens. This was further effort to approximate in-situ EGS conditions.

3.3.1 Microscope Analysis

Upon visual inspection, the block exhibited obvious isotropy (Fig. 3.2), that is, the granite crystallized deep within the pluton where it may have experienced low flow or no flow at all resulting in limited foliation. However, a microscope based foliation investigation of the Barre granite block was performed in order to identify any possible rift, grain, and hardway

planes. Foliation is an indicator of the alignment of minerals during cooling/crystallization, and is associated with the plane of greatest weakness due to weak discontinuities (Akesson et al., 2003). The identification of these planes helps to determine the proper specimen core orientation. Since the final experiment depends on water flow through the rock, the proper rock core orientation aligns the high permeability axis with the core axis. Additionally, the proper rock core orientation would encourage artificial fracture along the axis of the core. As supported in Sec 3.3, the rift would be most conducive to flow and fracture with greatest ease.

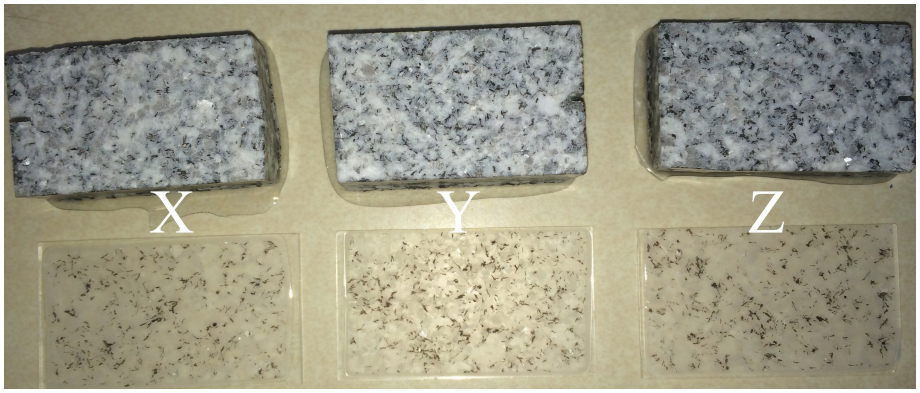

Figure 3.2: Hand specimens and thin sections for each axis of the granite block

The foliation investigation began with the extraction of three 30-micrometer thin sections (one orthogonal to each axis of the block (Fig. 3.2)). These thin sections were analyzed under a petrographic microscope for obvious signs of foliation (minerals exhibiting a predominant angle). Generally, micas were aligned at angles less than 45^o for the Y and Z axes Fig. 3.4a. Additionally, secondary weathering was observed within biotite angled 45^o from the horizontal (Fig. 3.4b). Although these two observations indicate possible foliation, a definite foliation/rift could not be determined. Therefore, a visual analysis of interstitial mica intrusions and an image analysis of the mica/biotite minerals were performed on the thin sections.

Upon visual inspection, interstitial mica inclusions were observed within the feldspar minerals. These may indicate the direction of original foliation. An example of one of these is shown in Fig. 3.4c. It was quickly observed that these exhibited a common alignment within the Y and Z planes. Angle observations were collected and averaged, resulting in 5^o in the Y plane and 22^o in the Z plane. A lack of interstitial mica was observed in the X plane.

3.3.2 Image Analysis

The image analysis involved scanning the thin sections (Fig. 3.2) and converting them to 8-bit images. A threshold was applied to isolate the mica/biotite minerals (Fig. 3.5 and a particle analysis/distribution was performed. The ImageJ software determined particle orientation and output statistics. For this analysis, particle orientations were binned into 20 deg tolerance bins and the mode was considered the most indicative of foliation orientation. The results showed a mode of 11 deg for the Y and Z axes, and a 0 deg orientation for the X axis. These results generally agree with the conclusions drawn in the analysis of interstitial mica. Generally, the deeper specimens are taken from rock formations the less foliation is observed (Fitz Osbourne, 1935). This block was extracted from the Barre granite quarry and so it is not unreasonable to assume limited foliation.

3.3.3 Foliation conclusion

A final plane of foliation was determined following the microscope and image analysis. The rift was oriented with the micas in the Y and Z axes. Following this result, the block was cored accordingly (Fig. 3.3) and the specimens were fractured lengthwise. The ease of creation of the lengthwise fracture (Fig. 3.6) further validated the decision to orient the cores as described.

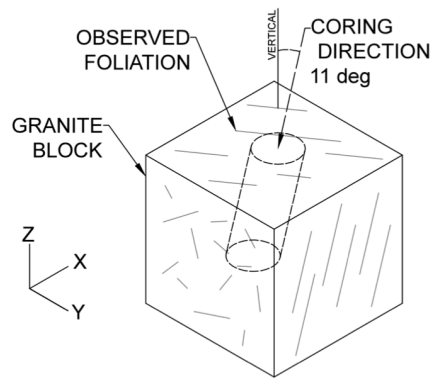

Figure 3.3: Orientation of the core with respect to the quarried block

Table 3.1: ImageJ Analysis Results

Thin Section	Mica Count	Total Area (pixels)	Average Size (pixels)	% Area	Mean	Mode
X	492	36772	74.74	4.32	4.12	0 (56)
Y	667	74773	112.10	5.57	1.80	11 (99)
Z	555	40381	72.76	4.03	2.27	11 (93)

3.3.4 XRD Analysis

An X-ray Diffraction (XRD) analysis was performed to confirm the constituent minerals within the granite rock. The results are shown in Table 3.2. The comparison of the XRD analysis performed for this study and two previous studies shows general rock composition agreement with slight discrepancies for quartz and albite (Nasseri et al., 2010; Thill et al., 1973). These discrepancies can be attributed to differences in specimen origin and analysis methods.

3.3.5 Density and Porosity

The density and porosity of the block were measured using traditional weight-volume relationships (Crawford, 2013). There are no ASTM standards available for determining bulk

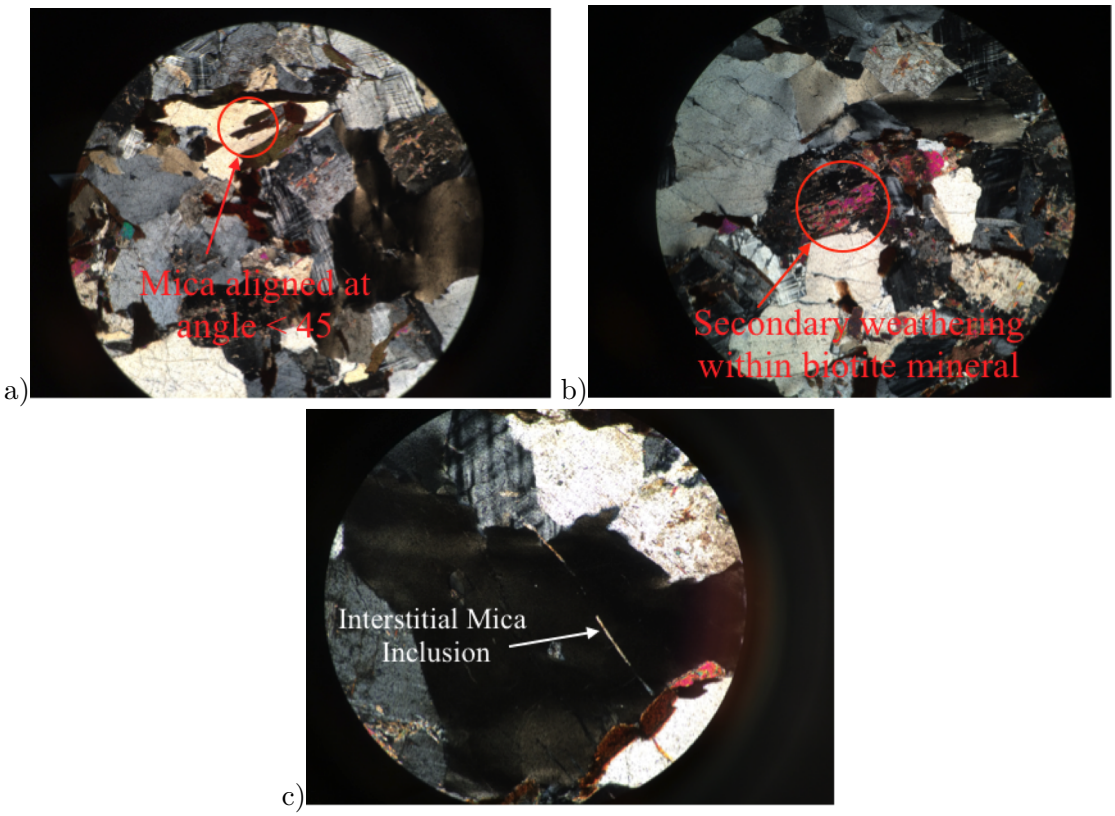

Figure 3.4: Microscope images of Y-axis thin section showing a) micas (4x magnification) b) biotite (4x magnification) and c) interstitial mica (10x magnification)

density or porosity of a rock core specimen; therefore, special care was taken during the estimation of these properties.

After cores were prepared according to Sec. 3.4.1, their weights were recorded. Following weighting, the cores were placed in a drying oven at 150^oF. Three weight measurements were recorded per day per specimen until the weight change was equal to or less than the precision of the scale (0.005 g) ($\approx 72hours$). Once the cores were fully dried, the length and diameter of each specimen was measured using a digital caliper. These measurements were repeated four times and average dry volume (V_{dry}) was calculated for each specimen. In addition to dimensions, the weight measurements were repeated to determine an average

Table 3.2: Barre granite mineral composition

Mineral	Current study (XRD) (%)	Thill, 1973 (Modal Analysis) (%)	Nasseri, 2010 (SEM)
Quartz	53	31.9	31
Albite	26	36.5	33.5
Microcline	8.2	17.8	30.5
Biotite	5.2	8.0	5
Muscovite	7.5	5.8	N/A

dry mass (m_{dry}) for each specimen. Dry bulk density was estimated using Eq. 3.1.

$$\rho = \frac{m}{V} \tag{3.1}$$

The saturated density and porosity were estimated using a vacuum saturation method. The dry cores were submerged in deionized water and placed under vacuum. Weights were measured once per day per specimen until the weight change was equal to or less than the precision of the scale (0.005 g) ($\approx 9days$). Once the cores were fully saturated, the length and diameter of each specimen was measured using a digital caliper. These measurements were repeated four times and an average volume (V_{sat}) was calculated for each specimen. In addition to dimensions, the weight measurements were repeated to determine an average saturated mass (m_{sat}). Saturated bulk density was estimated using Eq. 3.1.

Porosity was estimated by determining the volume of water present in the saturated specimens ($m_{sat} - m_{dry} = m_{water}$). The volume of the water was then estimated using Eq. 3.1. This method assumes the estimated volume of water represents the volume of pores. The advantages of this method are the simplistic process and non-specialized equipment. The disadvantage is that it only estimates the connected porosity. For this study, this value is sufficient.

Representative dry densities, saturated densities, and porosities for this granite block were calculated by averaging the values calculated for five specimens. Porosity was measured as 0.727 %, which matches reported porosity measurements for Barre Granite (0.51%) (Mariner et al., 2011). Dry and saturated densities were measured as 2.63 and 2.64 g/cc, which match generally accepted values for granite density.

3.4 Methodology

3.4.1 Specimen Preparation

Specimen diameter and length were both cored and cut to ≈38.5 mm. Following coring, the specimen ends were lapped parallel within 0.001 inch. Finally, a modified Brazilian test was used to fracture the specimens. The orientation of the fracture was selected using a mixture of thin-section image processing and microscopic observation methods detailed in Sec. 3.3. The resulting artificially fractured core is shown in Fig. 3.6. A negligible amount of rock matrix was lost during the fracturing process resulting in a perfectly fractured cylindrical core with parallel ends.

3.4.2 Experimental characteristics

The flow rate was carefully selected for these experiments. Preliminary steady-state experiments were performed on *intact granite specimens*. These tests showed that the maximum steady-state flow rate for the confining (30 MPa) and pore pressures (5 MPa) of interest was 0.000351 ml/min. Following these preliminary experiments, PHREEQC was used to model quartz and feldspar dissolution within a granite rock matrix. Although this model required broad assumptions for mineral grain size and surface area, it concluded that a low flow rate

(0.00005 ml/min) was necessary to achieve dissolution for the duration and temperature of the full-length experiments. A similar study performed by Savage et al. (1992) also supported the flow rate selected for this experiment (0.001 ml/min). Finally, the duration of the flow-through experiments was constrained by the volume of the pore pressure intensifier within the Autolab 1500. The volume of this intensifier is ≈20 ml, therefore, the longest uninterrupted experiment possible at 0.000351 ml/min was 40 days.

The duration of these experiments was carefully selected, but constrained by time limitations. Many past studies on the dissolution of quartz and feldspar ran experiments for more than 50 days (Morrow et al., 2001) up to 150 days (Ganor et al., 2005). For this study, the preliminary experiments were performed for 5 and 10 days, followed by a full-length experiment of 21 days.

The temperature of this experiment was constrained by limitations of the Autolab 1500. Ideally, these experiments should be performed at EGS temperatures (150-250^oC). The maximum temperature allowed for this equipment was 120^oC.

The confining pressures and pore pressures were carefully selected for these experiments. In a continued attempt to mimic EGS conditions, the confining pressures and pore pressures both match conditions present at roughly 3 km depth. Savage et al. (1992) used similar confining and pore pressures for their experiments on the EGS system in Rosmanowes, Cornwall, U.K. which lies at ≈ 2.5 km.

3.4.3 Experimental procedure

The experimental setup relied on consistent care to avoid contamination within the sample and the triaxial equipment. Prior to experimental initiation, all plumbing, pressure intensifiers, core holders, and reservoirs associated with the flow-through experiment were thoroughly washed with alcohol and hot deionized water. This experimental care effectively isolated the solvent used for the experiment (deionized water). Thus, any concentration of minerals observed in the ICP-MS analysis following the experiment could be attributed to mineral dissolution.

To initiate the experiment, the artificially fractured rock core was first saturated in deionized water under vacuum for 9 days. Following saturation, the core was prepared using a Viton™ sleeve and steady state core holders. The saturated/prepped core was then mounted into the hydrostatic vessel as shown in Fig. 3.7. 10 MPa of confining pressure was applied to the mounted sample before vacuum saturating pore pressure tubes with deionized water. This step ensured there was no air in the system i.e. the rock fracture and matrix were fully saturated prior to the initiation of flow.

A steady-state flow-through column-like experiment was performed on the specimen using the experimental setup shown in Fig. 3.8. The rock specimen was inserted into a vessel within the Autolab 1500 (Fig. 3.7b) where it was subjected to ≈30 MPa confining pressure and 5 MPa static internal pore pressure. Temperature of 120 ^oC was applied to the entire vessel. After 24 hours of equilibration, the flow of deionized water was initiated through the artificial fracture at a rate of ≈0.000351 ml/min. Detailed upstream and downstream pore pressure observations were recorded, and a parallel plate approximation (Polak et al., 2004) was used to estimate fracture aperture evolution (Eq. 3.2).

$$Q = \frac{\Delta P}{12\mu L} b^3 W \tag{3.2}$$

where, Q is flow rate $[m^3/s]$, ΔP is differential pressure $[Pa]$, μ is dynamic viscosity of the fluid $[Pa * s]$, L is the length of the core $[m]$, W is the diameter of the specimen $[m]$ and b is the fracture aperture $[m]$. It is important to note that by maintaining constant fluid flow rate, Q, and downstream pore pressure, the key proxy for fracture aperture change is the upstream pore pressure.

3.5 Results

3.5.1 Short Experiments Experiments

Short experiments were performed first to test and improve the proposed methodology. Resulting fracture aperture evolution for two injection flow rates is shown in Figures 3.9 and 3.10. As shown in Fig. 3.9, there is a clear trend of fracture aperture reduction with respect to time. This can be attributed to the dissolution of asperities on the surface of the fracture, resulting in fracture closing. However, it is clear that the fracture aperture is highly dependent on pore pressures. The first injection flow rate (0.000351 ml/min) resulted in an upstream pressure of ≈5.0 MPa. Fracture aperture during this step changed from 0.6 μm to 0.5 μm. Upon increase of flow rate in the following step (0.00175 ml/min) the upstream pore pressure increased to ≈5.2 MPa and fracture aperture closed from 0.75 μm to 0.6 μm.

3.5.2 Full Length Experiment

3.5.3 Aperture evolution as a function of pore pressure

A full 20-day experiment was performed following the completion of the preliminary experiment. This experiment was setup similar to the preliminary experiment; the Barre Granite specimen was artificially fractured and the working fluid was deionized water. For this experiment 30 MPa of confining pressure and 5 MPa of pore pressure were applied to the specimen. The experimental results followed the same trend as the preliminary 214 hour experiment until hour 375; fracture aperture decreased steadily with the presumed dissolution of fracture surface asperities (Fig. 3.11). However, a decrease of upstream pore pressure was observed after hour 375. This may be explained by etching (dissolution paths) on the fracture surface, resulting in more direct routes for water flow and a reduction in upstream/downstream pressure differential. Polak et al. (2004) observed a similar switch in permeability during a flow-through experiment on a limestone core (the study named them “wormholes"). These postulations were further investigated by running ICP-MS tests on the influent/effluent solutions and CT scanning the core.

The permeability of the specimen was evaluated using Darcy's Law (Eq. 3.3). This enabled the comparison of the experiment presented here with the closely related experiments performed by (Morrow et al., 2001). Permeability as a function of time is displayed in Fig. 3.12. The permeability decayed linearly with time from 2.1 mD ($2.1x10^{-15}m^2$) to 1.2 mD corresponding to a loss rate of 0.067 days^{-1} for the first 300 hours. These permeabilities compare closely to the ‘150-f’ results (fractured granite at effective pressure of 50 MPa and temperature150 ^oC) reported by Morrow et al. (2001) (Table 3.3). Morrow et al. (2001) observed $1x10^{-18}m^2$ at hour 300 and a permeability loss rate of 0.01 days^{-1}. This comparison encouraged the methodology used for the experiment presented here.

$$\frac{Q}{A} = \frac{k}{\mu}(dP/dx) \tag{3.3}$$

where Q is the volumetric flow rate (m^3/s), A is the cross-sectional area (m^2), k is the permeability (m^2), μ is the dynamic viscosity of water and (dP/dx) is the pressure gradient along the length of the specimen.

Table 3.3: Permeability comparison

Study	Current study	Morrow et al. 2010
Temperature ^oC	120	150
Fracture type	Tensile	Tensile
Confining Pressure (MPa)	30	150
Pore Pressure (MPa)	5	100
Effective Pressure (MPa)	25	50
Permeability @ hour 300 (m^2)	$1.2x10^{-15}$	$7x10^{-18}$
Loss rate ($days^{-1}$)	0.067	0.01

3.5.4 ICP-MS Analysis

The influent and effluent solutions were collected and analyzed for elemental concentrations using ICP-MS (Table 3.4). ICP-MS results indicate that incongruent feldspar (Albite and K-feldspar) dissolution is occurring. This conclusion is drawn from the increase in concentration for Si, Na, Ca, and K in the effluent and a minimal amount of Al. This supports the hypothesis that asperities propping the fracture open dissolve with time resulting in fracture aperture reduction. Additionally, the dissolution of Albite and K-feldspar supports the etching hypothesis.

The percent of rock dissolved was calculated using the dissolved mass of each element (mmol). $8.11x10^{-5}$% of the rock dissolved in the form of Si, Ca, Mg, K, and Na. This percentage corresponds to a volume of 0.036 mm^3.

Table 3.4: ICP-MS analysis results

Element	Effluent Conc.	LOD	Influent Conc. (ppm)	LOD	Increase	Dissolved mass (mmol)
Si	4.2	0.6	0.85	0.6	3.35	1.222e-3
Al	0.062	0.01	<0.4	0.4	N/A	N/A
Ca	5.6	0.2	2.9	1	2.7	6.903e-4
Mg	0.4	0.2	<1	1	N/A	N/A
K	3.1	0.2	<1	1	2.2	5.765e-4
Na	7	0.2	5.9	1	1.1	4.903e-4
Fe	ND	0.2	<1	1	N/A	N/A

3.5.5 Post experiment CT-Scan

The artificially fractured specimen was CT-scanned post-experiment as shown in Fig. 3.13. Although scans were not taken pre-experiment due to equipment availability, qualitative conclusions can be drawn using the post-experiment cross-sectional scans. Fig. 3.14 shows the specimen cross-section at 1/4 and 2/4 along the length of the specimen (where 4/4 would represent the downstream face of the core). These cross-sections show that the fracture faces no longer line up perfectly due to the loss of matter, which might be indicative of etching dissolution.

Future experiments will employ image analysis techniques for the comparison of pre and post experimental CT scans at several sections along the length of the core. This will enable the quantification of matter lost to dissolution.

3.6 Conclusions

A study was performed to improve existing experimental methodology that investigates the fracture aperture evolution within EGS. The modified experimental method is best de-

scribed as a steady-state flow-through column-like experiment on a cylindrical artificially fractured granite core rock. Preliminary experiments were used to develop and improve the final methodology used for the full-length experiments. Pore-pressure measurements recorded during the full-length experiment indicate a decreasing fracture aperture and permeability. In combination with ICP-MS results and CT scans, these results support the hypothesis that granite rock fractures are propped open by surface asperities, which will dissolve and reduce fracture aperture in the presence of deionized water. These findings emphasize the importance of rock-water interactions on granite rock permeability at high confining pressures and high temperatures.

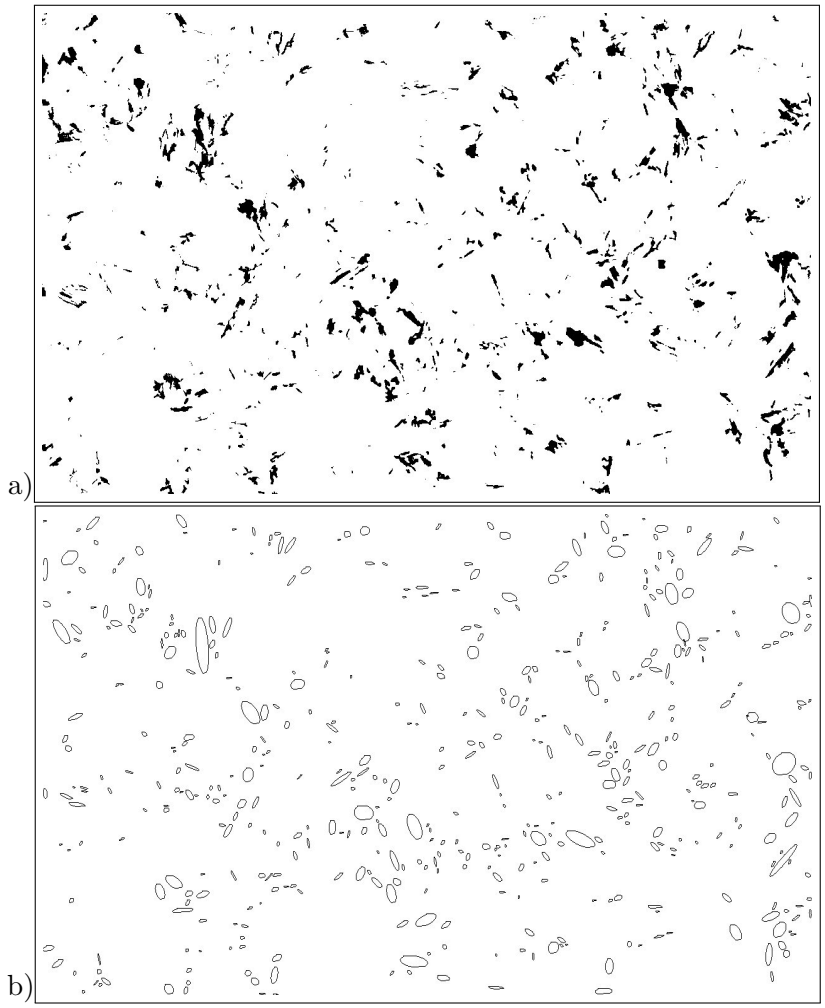

Figure 3.5: Sample images used during ImageJ analysis a) X axis mica distribution b) X axis particle orientation

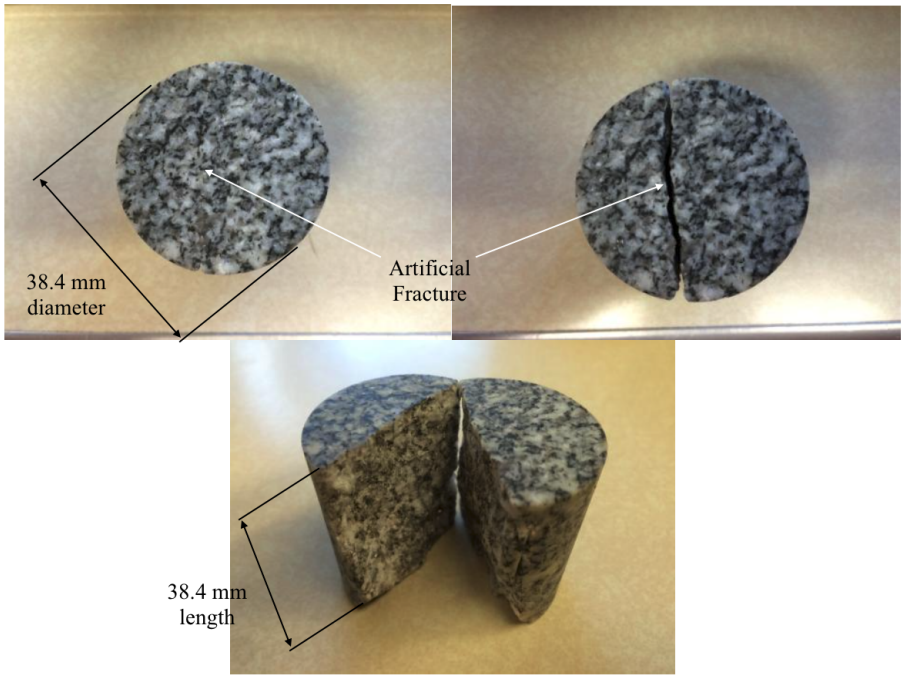

Figure 3.6: Images of core and artificial fracture

a)

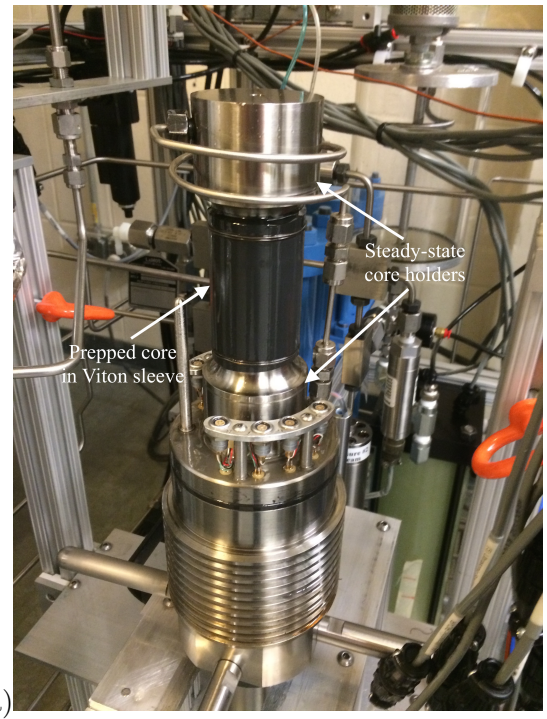

b)

Figure 3.7: a)Prepared core/core holder assembly mounted to base plug of vessel b)Autolab 1500

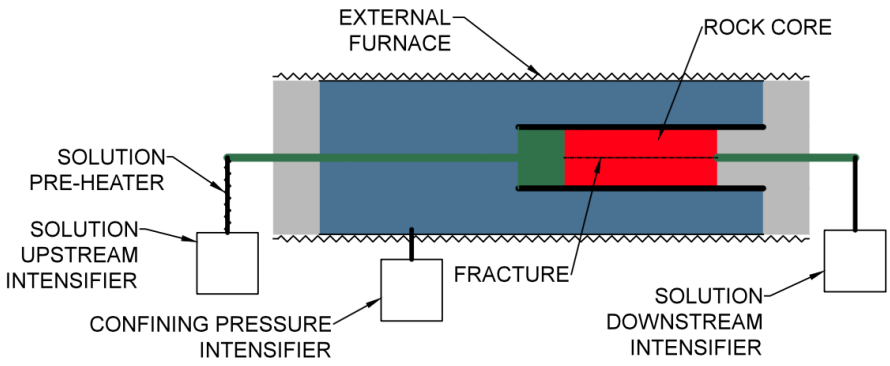

Figure 3.8: Schematic of the test cell (AutoLab 1500 vessel)

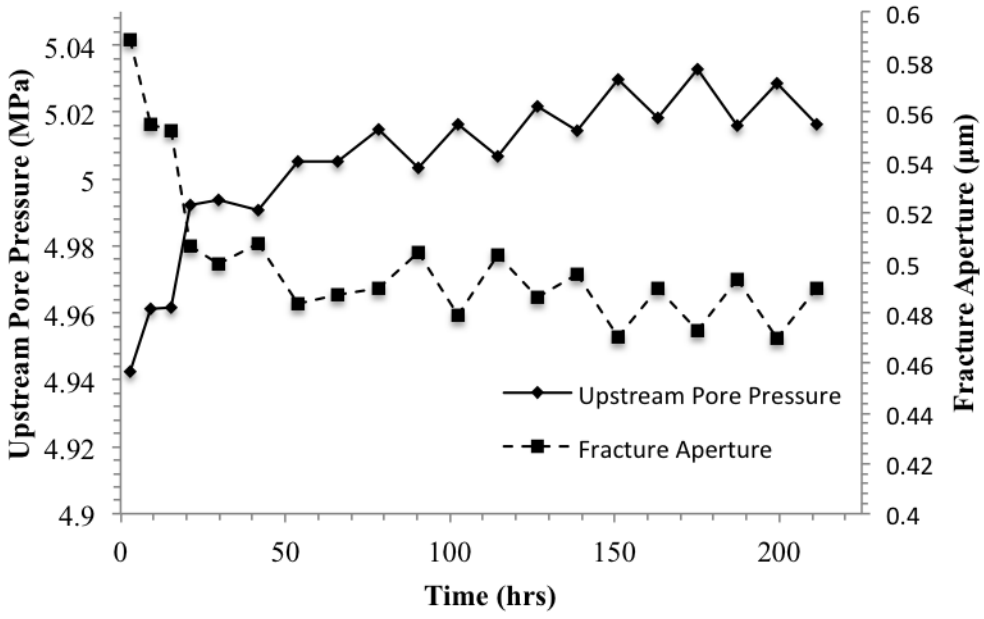

Figure 3.9: Upstream pore pressure and fracture aperture evolution during preliminary experiment 1 (flow rate = 0.000351 ml/min)

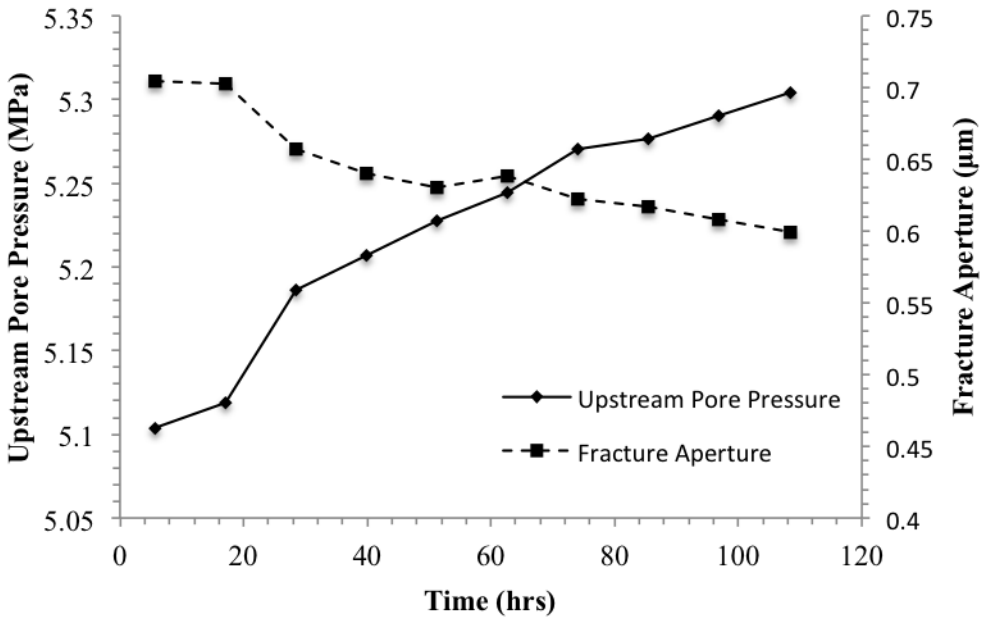

Figure 3.10: Upstream pore pressure and fracture aperture evolution during preliminary experiment 2 (flow rate = 0.00175 ml/min)

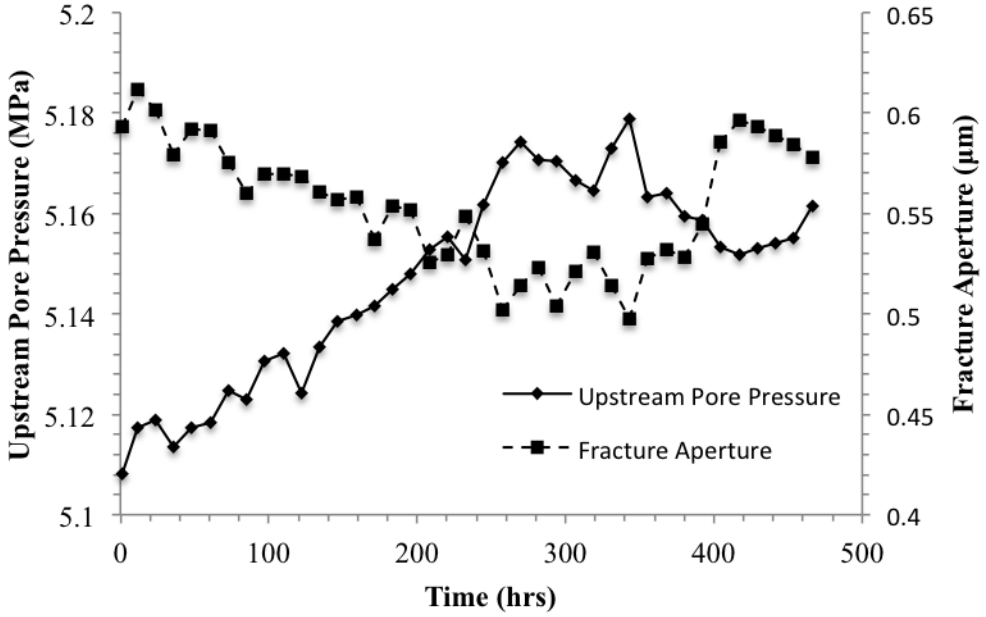

Figure 3.11: Upstream pore pressure and fracture aperture evolution during full length experiment (flow rate = 0.000351 ml/min)

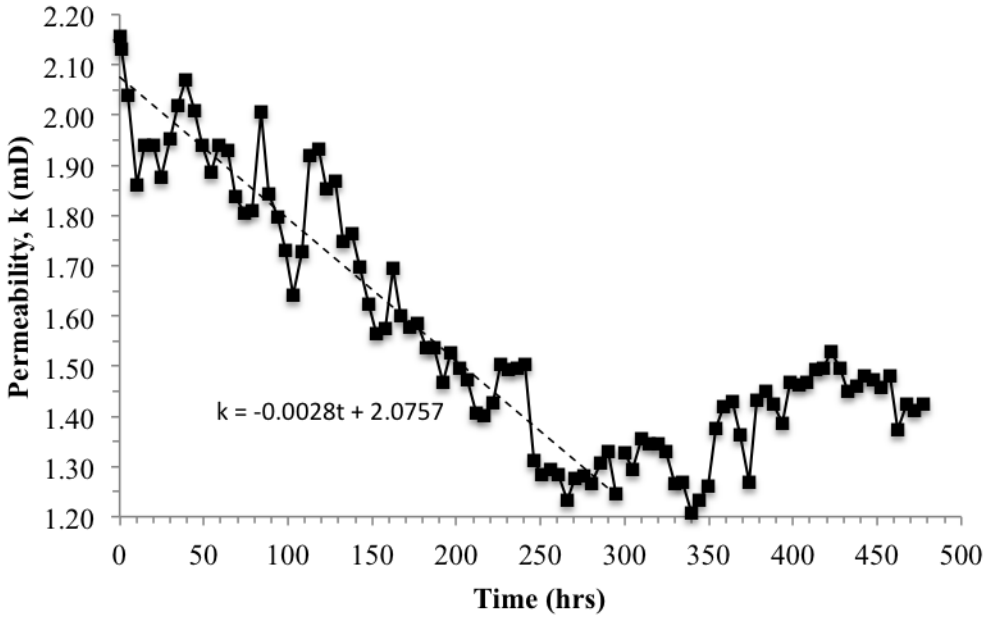

Figure 3.12: Permeability evolution during full length experiment (flow rate = 0.000351 ml/min)

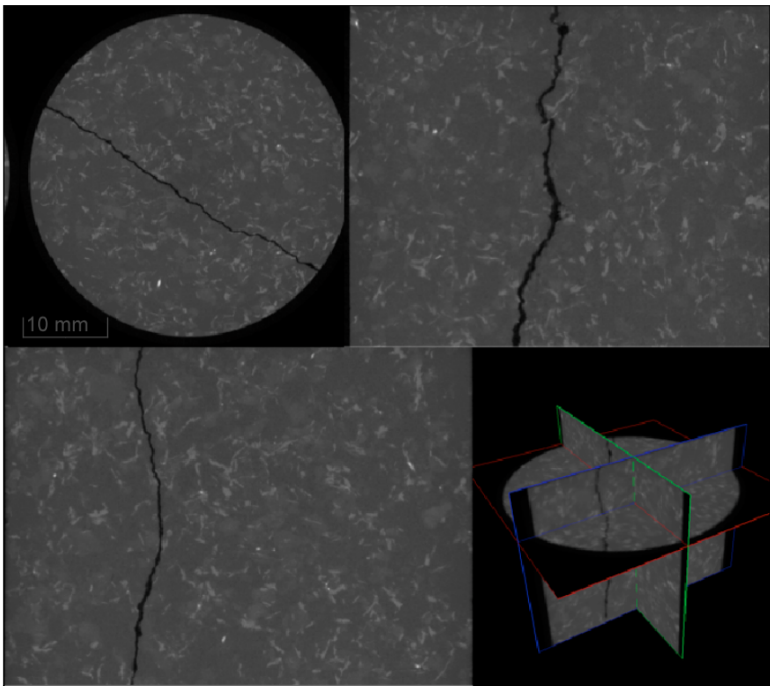

Figure 3.13: Oriented CT scans of specimen post-experiment

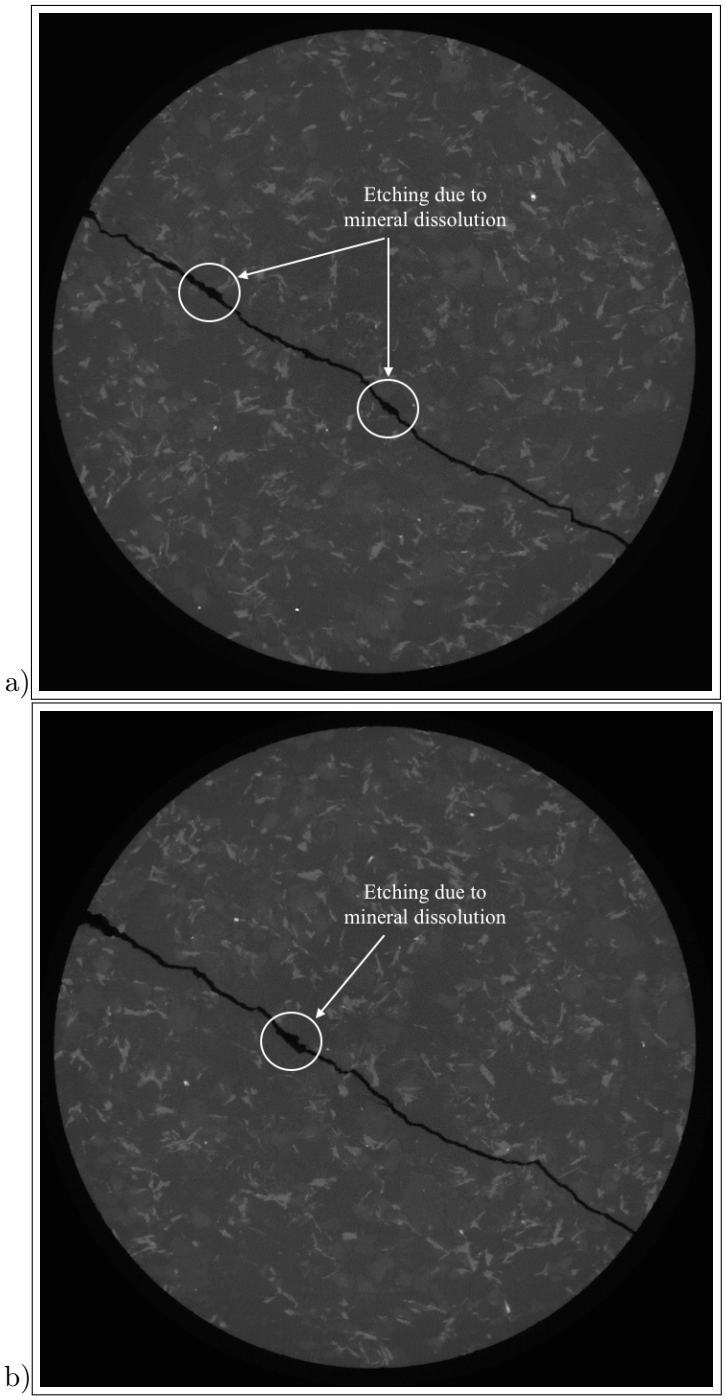

Figure 3.14: Cross-section CT scan showing etching dissolution at a) 1/4 length b) 2/4 length (0/4 = upstream face, 4/4 = downstream face)

Chapter 4

Conclusion

4.1 Thesis Summary

Geothermal energy represents a viable alternative to traditional fossil fuels. Shallow and deep geothermal energies have the potential to revolutionize indoor climate control and large scale electricity production, respectively. The key to both shallow and deep geothermal resource sustainability lies in increasing and maintaining performance. For shallow geothermal applications, this involves deepening our understanding of the thermal interaction between energy piles and surrounding soils. For deep geothermal applications, this involves deepening our understanding of rock-water interactions and permeability/fracture aperture evolution. This thesis attempted to add to the body of knowledge in the areas of shallow and deep geothermal energy.

The performance of energy piles with respect to construction specifications was investigated in this research (Chapter 2). The investigation involved the construction, calibration, and validation of a full-scale model. Construction and calibration of the model were both performed using available data extracted from an experimental group of energy piles located in Colorado Springs, CO. The intensive calibration resulted in a model that accurately ap-

proximated temperatures to within 3.6% of the field data (Sec. 2.10). Following calibration, the model was parameterized with respect to construction specifications (concrete cover, shank distance, and pile spacing). A performance metric was used to compare combinations of parameters (heat rejected - W/m). This allowed the study to quantify the performance increase/decrease with respect to construction specifications. Ultimately these combinations were optimized (Fig. 2.10). Results from the parameterization exercise validated the model and enabled the inspection of energy pile cross-sectional temperature/thermal strain distributions (Sec. 2.11.3). Cross-sectional thermal strain was demonstrated to vary across the core and around the perimeter of the energy piles. Based on the results from this study, it is clear that the performance on an energy pile depends strongly on the heat exchanger layout. An even heat exchanger layout is associated with a more even temperature/thermal strain distribution and a higher performance, while uneven heat exchanger layouts result in lower performance and varied cross-sectional thermal strain distribution.

The evolution of granite fracture apertures at EGS conditions was investigated in this research (Chapter 3). An experimental methodology addressed the combined hydro-thermo-mechanical-chemical processes that exist within EGS. The developed methodology is best described as a steady-state flow-through column-like experiment on an artificially fractured granite rock (Sec. 3.4). After the methodology was tested, modified, and improved, a full-length experiment was performed. Pore-pressure observations recorded during the full-length experiment indicated a decreasing fracture aperture and permeability (Sec. 3.5.2). In combination with ICP-MS results and CT scans, these results support the hypothesis: fracture surface asperities prop the fracture open and dissolve in the presence of deionized water resulting in decreased fracture aperture.

4.2 Future work

This thesis introduced ways to investigate both shallow and deep geothermal energy sustainability. Both studies presented here could be expanded upon in many different ways. The calibrated model used for the parametric investigation of energy piles could be adapted for several relevant studies. Similarly, the experimental methodology used for the investigation of fracture aperture analysis within EGS could be modified to study more sustainable working fluids.

The calibrated model used for the parametric investigation of energy piles can be modified for two relevant studies. The study presented within this thesis showed the variable temperature/strain distribution within an energy pile during a Thermal Response Test (Chapter 2). Future studies should adapt this model to investigate the evolution of the cross-sectional strain due to cyclic loadings (between heat rejection and heat extraction). In order to perform these studies, the model boundary conditions would need to be modified. Namely, the variable inlet temperature would need to be adjusted to represent true cyclic loading. These studies may yield additional insight for the estimation of thermal stress and strain using field measured observations. Another relevant study should investigate long-term behavior of energy piles (50+ years). In order to accurately investigate long-term energy pile behavior using the model presented in this thesis, not only would the model boundary conditions need to be drastically modified, but the mesh and solver would also require fine tuning. The variable temperature subsurface temperature boundary condition is currently variable with depth, but for the proposed investigation it would need to be variable with time as well. The inlet temperature would need to represent a true energy pile. This means the inlet temperature would need to be a function of the atmospheric temperature. In the case of a functional inlet temperature, the energy pile would

only be activated when necessary. In order to model this behavior, flow rate would need to be turned on and off periodically. Time-dependent modeling does not cater to this type of periodic boundary condition (especially for fluid flow), and thus requires significant computational time and resources. It may be prudent to investigate alternative ways to model the long-term pile behavior at reduced computational cost. Perhaps adjusting a different model parameter could achieve the same effect as adjusting fluid flow (e.g. heat exchanger thermal conductivity may need to be adjusted from 0.2 - 0 $W/(m*k)$ to 'turn the pile off'). Or it may be necessary to build and calibrate a two dimensional model to the model used for this thesis.

The experimental methodology used for the investigation of fracture aperture analysis within EGS should first be further validated, and second it should be modified to study more sustainable working fluids. The results discussed within this thesis provided insight into the evolution of fracture aperture within Enhanced Geothermal Systems. Although the results and analyses support the hypothesis, they are not conclusive due to questionable aperture behavior at extended experimental times (300 hours+). Therefore, a replicate experiment should be performed to determine whether this behavior is a result of the water-rock interactions (specifically the development of etching on the fracture surface), and not due to possible experimental error. Following a replicate, the results should support or contradict the original experiment. At that point, a follow up investigation should be developed to study the interactions of salts on the dissolution of quartz and feldspar minerals. This study should stem from existing studies performed on the effect of salt presence on mineral dissolution rates and kinetics Dove (1999); Dove and Nix (1994); Gautier et al. (1994); Worley (1994).

Chapter 5
Comprehensive Bibliography

Bibliography

Abdelaziz, S. L., Olgun, C. G., and Martin, J. R. (2015). Equivalent energy wave for long-term analysis of ground coupled heat exchangers. *Geothermics*, 53:67–84.

Abdelaziz, S. L., Ozudogru, T. Y., Olgun, C. G., and Martin, J. R. (2014). Multilayer finite line source model for vertical heat exchangers. *Geothermics*, 51:406–416.

Akesson, U., Stigh, J., Lindqvist, J., and Goransson, M. (2003). The influence of foliation on the fragility of granitic rocks , image analysis and quantitative microscopy. *Engineering Geology*, 68:275–288.

Barnabe, Y. (1986). The Effective Pressure Law for Permeability in Chelmsford Granite and Barre Granite. *Journal of Rock Mechanics, Mineral Sci. and Geomechanics*, 23(3):267–275.

Barnard, A. C., Hunt, W. A., Timlake, W. P., and Varley, E. (1966). A theory of fluid flow in compliant tubes. *Biophysical Journal*, 6:717–724.

Bourne-Webb, P., Pereira, J., Bowers, G., Mimouni, T., Loveridge, F., Burlon, S., Olgun, C. G., McCartney, J. S., and Sutman, M. (2014). Design tools for thermoactive geotechnical systems. *DFI Journal: The Journal of the Deep Foundations Institute*, 8(2):121–129.

Bourne-Webb, P. J., Amatya, B., Soga, K., Amis, T., Davidson, C., and Payne, P. (2009). Energy pile test at Lambeth College, London: geotechnical and thermodynamic aspects of pile response to heat cycles. *Geotechnique*, 59(3):237–248.

Brace, W. (1980). Permeability of crystalline and argillaceous rocks. *International Journal of Rock Mechanics and Mining Sciences & Geomechanics Abstracts*, 17(5):241–251.

Brandl, H. (2006). Energy foundations and other thermo-active ground structures. *Géotechnique*, 56(2):81–122.

Caulk, R. and Ghazanfari, E. (2015). Investigation of construction specification effects on energy pile efficiency. In *Proceedings of the International Foundations Conference and Equipment Exposition (IFCEE 2015)*, pages 1648–1657, San Antonio, TX. Mar. 17-21. ASCE.

Caulk, R., McCartney, J., and Ghazanfari, E. (2014). Calibration of a geothermal energy pile model. In *Proceedings of the COMSOL Boston 2014 Conference*, Boston, MA. COMSOL.

Cecinato, F. and Loveridge, F. (2015). Influences on the thermal efficiency of energy piles. *Energy*, 82:1021–1033.

Crawford, K. M. (2013). *Determination of bulk density of rock core using standard industry methods*. PhD thesis, Michigan Technological University.

Dove, P. M. (1999). The dissolution kinetics of quartz in aqueous mixed cation solutions. *Geochmica et Cosmochimica Acta*, 63(22):3715–3727.

Dove, P. M. and Nix, C. J. (1994). The influence of the alkaline earth cations , magnesium , calcium , and barium on the dissolution kinetics of quartz A = CsXrl2 Â° e (k ˜). *Geochimica et Cosmochimica Acta*, 61(16):3329–3340.

EIA (2011). Annual Energy Review. Technical report, Energy Information Administration.

Eppelbaum, L., Kutasov, I., and Pilchin, A. (2014). Thermal Properties of Rocks and Density of Fluids. In *Applied Geothermics*, Lecture Notes in Earth System Sciences, pages 99–142. Springer-Verlag Berlin Heidelberg, Berlin, Heidelberg.

Evans, K. F., Cornet, F. H., Hashida, T., Hayashi, K., Ito, T., Matsuki, K., and Wallroth, T. (1999). Stress and rock mechanics issues of relevance to HDR/HWR engineered geothermal systems: Review of developments during the past 15 years. *Geothermics*, 28:455–474.

Fitz Osbourne, F. (1935). Rift, Grain, and Hardway in some Pre-Cambian Granites, Quebec. *Economic Geology*, 30:540–551.

Ganor, J., Roueff, E., Erel, Y., and Blum, J. D. (2005). The dissolution kinetics of a granite and its minerals Implications for comparison between laboratory and field dissolution rates. *Geochimica et Cosmochimica Acta*, 69(3):607–621.

Gao, J., Zhang, X., Liu, J., Li, K., and Yang, J. (2008). Numerical and experimental assessment of thermal performance of vertical energy piles: An application. *Applied Energy*, 85(10):901–910.

Gashti, E. H. N., Uotinen, V. M., and Kujala, K. (2014). Numerical modelling of thermal regimes in steel energy pile foundations: A case study. *Energy and Buildings*, 69:165–174.

Gautier, J.-M., Oelkers, E. H., and Schott, J. (1994). Experimental study of K-feldspar dissolution rates as a function of chemical affinity at 150Â°C and pH 9. *Geochimica et Cosmochimica Acta*, 58(21):4549–4560.

Ghasemi-Fare, O. and Basu, P. (2013). A practical heat transfer model for geothermal piles. *Energy and Buildings*, 66:470–479.

Ghassemi, A. (2012). A Review of Some Rock Mechanics Issues in Geothermal Reservoir Development. *Geotechnical and Geological Engineering*, 30(3):647–664.

Ghassemi, A., Nygren, A., and Cheng, A. (2008). Effects of heat extraction on fracture aperture: A poro-thermoelastic analysis. *Geothermics*, 37:525–539.

Ghassemi, A. and Suresh Kumar, G. (2007). Changes in fracture aperture and fluid pressure due to thermal stress and silica dissolution/precipitation induced by heat extraction from subsurface rocks. *Geothermics*, 36:115–140.

Ghassemi, A., Tarasovs, S., and Cheng, A. (2005). Integral equation solution of heat extraction-induced thermal stress in enhanced geothermal reservoirs. *International Journal for Numerical and Analytical Methods in Geomechanics*, 29(8):829–844.

Ghassemi, A. and Zhang, Q. (2004). A transient fictitious stress boundary element method for porothermoelastic media. *Engineering Analysis with Boundary Elements*, 28:1363–1373.

Ghassemi, A. and Zhang, Q. (2006). Porothermoelastic Analysis of the Response of a Stationary Crack Using the Displacement Discontinuity Method.

Ghassemi, A. and Zhou, X. (2011). A three-dimensional thermo-poroelastic model for fracture response to injection/extraction in enhanced geothermal systems. *Geothermics*, 40(1):39–49.

GSHPA (2012). Thermal Pile Design , Installation and Materials Standards. Technical Report October 2012, Ground Source Heat Pump Association.

Hakami, E. and Larsson, E. (1996). Aperture Measurements and Flow Experiments on a Single Natural Fracture. *Journal of Rock Mechanics, Mineral Sci. and Geomechanics*, 33(4):395–404.

Hamada, Y., Saitoh, H., Nakamura, M., Kubota, H., and Ochifuji, K. (2007). Field performance of an energy pile system for space heating. *Energy and Buildings*, 39(5):517–524.

Jalaluddin and Miyara, A. (2014). Performance investigation of multiple-tube ground heat exchangers for ground-source heat pump. *American Journal of Energy Engineering*, 2(5):103–107.

Kaltreider, C., Krarti, M., and McCartney, J. S. (2015). Heat transfer analysis of thermoactive foundations. *Energy and Buildings*, 86:492–501.

Koh, J., Roshan, H., and Rahman, S. S. (2011). A numerical study on the long term thermoporoelastic effects of cold water injection into naturally fractured geothermal reservoirs. *Computers and Geotechnics*, 38(5):669–682.

Kohl, T., Evansi, K., Hopkirk, R., and Rybach, L. (1995). Coupled hydraulic, thermal and mechanical considerations for the simulation of hot dry rock reservoirs. *Geothermics*, 24:345–359.

Kranz, R. L., Frankel, A. D., Engelder, T., and Scholz, C. H. (1979). The Permeability of Whole and Jointed Barre Granite. *Journal of Rock Mechanics, Mineral Sci. and Geomechanics*, 16(3):225–234.

Laloui, L. and Di Donna, A. (2013). *Energy Geostructures: Innovation in Unerground Engineering*. Wile-ISTE.

Laloui, L., Nuth, M., and Vulliet, L. (2006). Experimental and numerical investigations of the behaviour of a heat exchanger pile. *International Journal for Numerical and Analytical Methods in Geomechanics*, 30:763–781.

Li, M. and Lior, N. (2014). Comparative Analysis of Power Plant Options for Enhanced Geothermal Systems (EGS). *Energies*, 7(12):8427–8445.

Loveridge, F. and Powrie, W. (2012). Performance of piled foundations used as heat exchangers. In *18th International Conference for Soil Mechanics and Geotechnical Engineering*, pages 3371–3374. ICE Geotech Eng.

Loveridge, F. and Powrie, W. (2013). Temperature response functions (G-functions) for single pile heat exchangers. *Energy*, 57:554–564.

Mariner, P. E., Lee, J. H., Hardin, E. L., Hansen, F. D., Freeze, G. A., Lord, A. S., Goldstein, B., and Price, R. H. (2011). Granite Disposal of U . S . High-Level Radioactive Waste. Technical Report August 2011, Sandia National Laboratory.

McCartney, J. S., Murphy, K. D., and Henry, K. S. (2015). Response of an energy foundation to temperature fluctuations. In *Proceedings of the International Foundations Conference and Equipment Exposition (IFCEE 2015)*, pages 1691–1700, San Antonio, TX. Mar. 17-21. ASCE.

Mimouni, T. and Laloui, L. (2014). Towards a secure basis for the design of geothermal piles. *Acta Geotechnica*, 9(3):355–366.

MIT Report (2006). The Future of Geothermal Energy : Impact of Enhanced Geothermal Systems (EGS) on the United States in the 21st Century: an assessment. Technical Report November 2006, Idaho National Laboratory, Cambridge, MA.

Morino, K. and Oka, T. (1994). Study on heat exchanged in soil by circulating water in a steel pile. *Energy and Buildings*, 21(1):65–78.

Morrow, C. A., Moore, D. E., and Lockner, D. A. (2001). Permeability reduction in granite under hydrothermal conditions. *Geopphysical Research*, 106:30,551–30,560.

Murphy, K. D. and McCartney, J. S. (2015). Seasonal response of energy foundations during building operation. *Geotechnical and Geological Engineering*, 33(2):343–356.

Murphy, K. D., McCartney, J. S., and Henry, K. S. (2015). Evaluation of thermo-mechanical and thermal behavior of full-scale energy foundations. *Acta Geotechnica*, 10(2):179–195.

Mustafa Omer, A. (2008). Ground-source heat pumps systems and applications. *Renewable and Sustainable Energy Reviews*, 12(2):344–371.

Nasseri, M. H. B., Grasselli, G., and Mohanty, B. (2010). Fracture toughness and fracture roughness in anisotropic granitic rocks. *Rock Mechanics and Rock Engineering*, 43:403–415.

Oda, M., Takemura, T., and Aoki, T. (2002). Damage growth and permeability change in triaxial compression tests of Inada granite. *Mechanics of Materials*, 34(6):313–331.

Olgun, C. G., Martin, J., Abdelaziz, S., Iovino, P. L., Catalbas, F., Elks, C., Fox, C., and Gouvin, P. (2012). Field testing of energy piles at Virginia Tech. In *Proceedings from the 37th Annual Conference on Deep Foundations*, Houston, TX.

Ozudogru, T., Olgun, C., and Senol, A. (2014). 3D numerical modeling of vertical geothermal heat exchangers. *Geothermics*, 51:312–324.

Park, H., Lee, S., Yoon, S., and Choi, J. (2013). Evaluation of thermal response and performance of PHC energy pile: Field experiments and numerical simulation. *Applied Energy*, 103:12–24.

Polak, A., Elsworth, D., Liu, J., and Grader, A. S. (2004). Spontaneous switching of permeability changes in a limestone fracture with net dissolution. *Water Resources Research*, 40(3):n/a–n/a.

Savage, D., Bateman, K., and Richards, H. (1992). Granite-water interactions in a flow-through experimental system with applications to the Hot Dry Rock geothermal system at. *Applied Geochemistry*, 7:223–241.

Singurindy, O. and Berkowitz, B. (2005). The role of fractures on coupled dissolution and precipitation patterns in carbonate rocks. *Advances in Water Resources*, 28(5):507–521.

Suryatriyastuti, M. E., Mroueh, H., and Burlon, S. (2012). Understanding the temperature-induced mechanical behaviour of energy pile foundations. *Renewable and Sustainable Energy Reviews*, 16:3344–3354.

Tarasovs, S. and Ghassemi, A. (2012). On the Role of Thermal Stress in Reservoir Stimulation. In *Proc. 37th Workshop on Geothermal Reservoir Engineering*, Stanford, CA. Stanford University.

Thill, R. E., Bur, T. R., and Steckley, R. C. (1973). Velocity anisotropy in dry and saturated rock spheres and its relation to rock fabric. *International Journal of Rock Mechanics and Mining Sciences & Geomechanics Abstracts*, 10(6):535–557.

Wang, W., Regueiro, R. A., and McCartney, J. S. (2014). Coupled axissymmetric thermo-poro-elasto-plastic finite element analysis of energy foundation centrifuge experiments in partially saturated silt. *Geotechnical and Geological Engineering*, 33(2):373–388.

Wood, C. J., Liu, H., and Riffat, S. B. (2009). Use of energy piles in a residential building , and effects on ground temperature and heat pump efficiency. *Geotechnique*, 59(3):287–290.

Worley, W. G. (1994). *Dissolution Kinetics and Mechanisms in Quartz and Granite-water Systems*. PhD thesis, Massachusetts Intitute of Technology.

Xiong, Y., Hu, L., and Wu, Y.-s. (2013). Coupled Geomechanical and Reactive Geochemical Simulations for Fluid and Heat Flow in Enhanced Geothermal Reservoirs. In

Thirty-Eighth Workship on Geothermal Reservoir Engineering, Stanford, CA. Stanford Universitty.

Xu, T., Sonnenthal, E., Spycher, N., Pruess, K., Brimhall, G., and Apps, J. (2001). Modeling multiphase non-isothermal fluid flow and reactive geochemical transport in variably saturated fractured rocks: 2. Applications to supergene copper enrichment and hydrothermal flows. *American Journal of Science*, 301:34–59.

Yasuhara, H. and Elsworth, D. (2006). A numerical model simulating reactive transport and evolution of fracture permeability. *International Journal for Numerical and Analytical Methods in Geomechanics*, 30(10):1039–1062.